Planetary2D Validation Manual

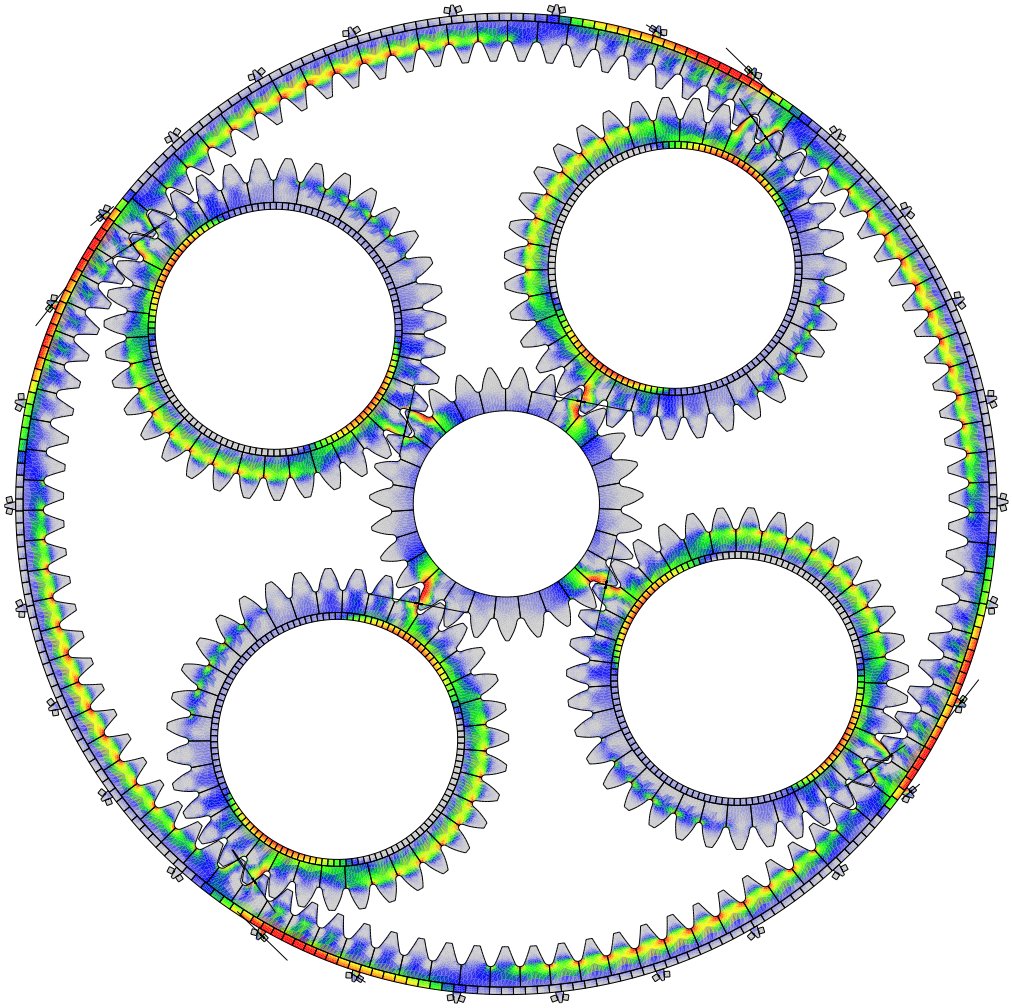

Advanced Numerical Solutions
Hilliard OH

April 25, 2006

Contents

Preface **ix**

1 Calculating the dynamic load factor **1**
1.1 Calculating the time step . . . 1
1.2 The setup menu . . . 3
1.3 Analysis and Results . . . 5
1.3.1 Calculating the Dynamic load factor . . . 9

2 Effect of Pin position errors on the planet load distribution **13**
2.1 Effect of pin position errors on a 4 pinion planetary system . . . 15
2.2 Effect of pin position errors on a 3 pinion planetary system . . . 20
2.3 Effect of pin position errors on a 5 pinion planetary system . . . 25
2.4 Summary . . . 30

3 Comparison of Experimental results and results obtained from Calyx **31**

4 Dynamic Analysis **45**
4.0.1 Introduction . . . 45
4.0.2 Free Vibration Modes . . . 45
4.0.3 Validation of Impulse Response Functions . . . 46
4.0.4 Dynamic Response Under Operating Conditions . . . 47
4.0.5 Results and Discussion . . . 48

5 Housing Vibration Spectra **57**
5.1 Introduction . . . 57
5.2 Theoretical Development . . . 57
5.3 Validation . . . 58
5.4 Conclusion . . . 63

6 Load Sharing Analysis **65**
6.1 Introduction . . . 65
6.2 Modeling and Equations of Motion . . . 65
6.3 Load Sharing Calculation . . . 67
6.3.1 Load Sharing Statistics . . . 69
6.4 Implementation . . . 69
6.5 Comparision with Lumped Parameter Model . . . 69

List of Figures

1.1 Graph showing the dynamic maximum principal normal stresses (s1) and minimum principal normal stresses (s3) against time for the fillet surface of the sun gear, measured by Surfage Gage 1. The results are obtained from the file GAGES.DAT. 5
1.2 Graph showing the pinion bearing tangential displacement against time for dynamic analysis. The tangential displacement at each instant of time is given in Column no.3 of the PINION1BRGRES.DAT file. 7
1.3 Graph showing the housing moments against time for dynamic analysis. The moment about the Z-axis for each time instant is given in column no.13 of the HOUSINGRES.DAT file 8
1.4 Graph showing the dynamic tooth load against time. The plot is obtained using the load values from column nos.6, 10, 11 and 12 from the LOADS.DAT file. . . 9
1.5 Graph showing the static tooth load against time using the TOOTHLOAD command. 11

2.1 The pinion assembly errors. 14
2.2 Load distribution on each pinion for a 4 pinion planetary system with no pin position errors. 15
2.3 Load distribution on each pinion for a 4 pinion planetary system with pin position error applied on Pinion 2. 16
2.4 Load distribution on each pinion for a floating sun, 4 pinion planetary system with pin position error applied on Pinion 2. 17
2.5 Load distribution on each pinion for a floating carrier, 4 pinion planetary system with pin position error applied on Pinion 2. 18
2.6 Load distribution on each pinion for a floating sun and carrier, 4 pinion planetary system with pin position error applied on Pinion 2. 19
2.7 Load distribution on each pinion for a 3 pinion planetary system with no pin position errors. 20
2.8 Load distribution on each pinion for a 3 pinion planetary system with pin position error applied on Pinion 2. 21
2.9 Load distribution on each pinion for a floating sun, 3 pinion planetary system with pin position error applied on Pinion 2. 22
2.10 Load distribution on each pinion for a floating carrier, 3 pinion planetary system with pin position error applied on Pinion 2. 23
2.11 Load distribution on each pinion for a floating sun and carrier, 3 pinion planetary system with pin position error applied on Pinion 2. 24
2.12 Load distribution on each pinion for a 5 pinion planetary system with no pin position errors. 25
2.13 Load distribution on each pinion for a 5 pinion planetary system with pin position error applied on Pinion 2. 26

2.14 Load distribution on each pinion for a floating sun, 5 pinion planetary system with pin position error applied on Pinion 2. 27
2.15 Load distribution on each pinion for a floating carrier, 5 pinion planetary system with pin position error applied on Pinion 2. 28
2.16 Load distribution on each pinion for a floating sun and carrier, 5 pinion planetary system with pin position error applied on Pinion 2. 29

3.1 Planetary gear set model created through Multyx for comparing results. 32
3.2 Contours of maximum principal normal stress in the sun gear. 33
3.3 Contours of maximum principal normal stress in the ring gear and the pinion. . . 34
3.4 Variation of maximum principal normal stress in the planetary gear system. . . . 35
3.5 Variation of minimum principal normal stress in the planetary gear system. . . . 36
3.6 Closeup of the minimum principal normal stress variation near one of the splines on the ring gear's outer diameter. 37
3.7 Experimental results for stress obtained from strain gages mounted in the fillet on the loaded side of the ring gear tooth. Experimental data is from Krantz [2]. . 38
3.8 Computational predictions of fillet stress on the loaded side of the ring gear tooth. 38
3.9 Experimental results for stress obtained from strain gages mounted in the fillet on the unloaded side of the ring gear tooth. Experimental data is from Krantz [2] 39
3.10 Computational predictions of fillet stress on the unloaded side of the ring gear tooth. 39
3.11 Experimental results for stress obtained from strain gages mounted in the fillet on the loaded side of the sun gear tooth. Experimental data is from Krantz [2]. . 40
3.12 Computational predictions of fillet stress on the loaded side of the sun gear tooth. 40
3.13 Experimental results for stress obtained from strain gages mounted in the fillet on the unloaded side of the ring gear tooth. Experimental data is from Krantz [2]. 41
3.14 Computational predictions of fillet stress on the unloaded side of the ring gear tooth. 41

4.1 Matlab program for computing vibration modes of a planetary system. 50
4.2 Driving point response – sun x-translation. 51
4.3 Frequency spectra of sun x-translation. 52
4.4 Frequency spectra of sun θ_z rotation. 53
4.5 Frequency spectra of pinion radial translation. 54
4.6 Frequency spectra of pinion rotation. 55
4.7 Frequency spectra of ring gear translation. 56

5.1 Force on Spline 1 over one complete rotation of the carrier 59
5.2 Force on Spline 1 as a planet passes the spline 59
5.3 Force spectra on spline 1, 0-1000 Hz 60
5.4 Force on Spline 1 around the zeroth mesh harmonic. 61
5.5 Force on Spline 1 around the first mesh harmonic. 62
5.6 Force on Spline 1 around the second mesh harmonic. 63

6.1 Lumped parameter model of the planetary gears and system coordinates. 66
6.2 Excitation due to linear interference of ϵ at the planet i mesh 68
6.3 Software for load sharing analysis. 71

List of Tables

1.1 Setup menu 4
1.2 Surface gage data for extracting the plot shown in Figure 1.1 6
1.3 Load sensor data for extracting the plot shown in Figure 1.4 10
1.4 Tooth load data for extracting the plot shown in Figure 1.5 10

2.1 Pin position error menu 16
2.2 Load distribution values for a 4 pinion planetary system 19
2.3 Load distribution values for a 3 pinion planetary system 24
2.4 Load distribution values for a 5 pinion planetary system 29

4.1 Natural frequencies (Hz). $N = 4$ and free-free boundary conditions. 46
4.2 Natural frequency comparison for the four planet gear system. 47
4.3 Natural frequency comparison for the four planet gear system. 48
4.4 Geometry parameters to compute ring gear natural frequencies. 49
4.5 Ring gear modes and natural frequencies. 49

5.1 Gear Parameters for example system 58
5.2 Tooth harmonics and sidebands predicted by the theoretical model 61
5.3 Tooth harmonics and sidebands predicted by the theoretical model 62
5.4 Tooth harmonics and sidebands predicted by the theoretical model 63

6.1 Planet load sharing in the Helicopter gearbox due to sun axis error 70

Preface

The Planetary2D computer program has been under development for many years, and is finally available for use by the gearing community. I have received active support and encouragement from many people. I would especially like to thank Timothy Krantz of the Army Research Laboratory at the NASA Glenn Research Center for his support and encouragement.

Sandeep Vijayakar, Hilliard OH
December 2002

Chapter 1

Calculating the dynamic load factor

Load the file `dynamicrun.ses` from the Working directory. The data for this model is similar to the example of the dynamic case given in the Users manual.

1.1 Calculating the time step

Let,

$$
\begin{aligned}
\omega_s &= \text{Angular speed of the Sun gear in rad/sec} \\
\omega_c &= \text{Angular speed of the Carrier in rad/sec} \\
\omega_p &= \text{Angular speed of the Pinion gear in rad/sec} \\
\omega_R &= \text{Angular speed of the Ring gear in rad/sec} \\
RPM_s &= \text{Speed of the sun gear in RPM} \\
RPM_c &= \text{Speed of the carrier in RPM} \\
RPM_p &= \text{Speed of the pinion in RPM} \\
RPM_R &= \text{Speed of the ring gear in RPM} \\
N_s &= \text{Number of teeth on the sun gear} \\
N_p &= \text{Number of teeth on the pinion gear} \\
N_R &= \text{Number of teeth on the ring gear} \\
\Delta_T &= \text{Time Step} \\
T_{cycle} &= \text{Tooth Cycle time} \\
n_{steps} &= \text{Total number of steps per tooth cycle}
\end{aligned}
$$

The following relationships are used to determine the time step required for dynamic cases.

$$(\omega_s - \omega_c)N_s = -(\omega_p - \omega_c)N_p = -(\omega_R - \omega_c)N_R$$

$$T_{cycle} = |\frac{2\pi}{(\omega_s - \omega_c)N_s}| = |\frac{2\pi}{(\omega_p - \omega_c)N_p}| = |\frac{2\pi}{(\omega_R - \omega_c)N_R}|$$

$$T_{cycle} = |\frac{60}{(RPM_s - RPM_c)N_s}| = |\frac{60}{(RPM_p - RPM_c)N_p}| = |\frac{60}{(RPM_R - RPM_c)N_R}|$$

$$\Delta_T = \frac{T_{cycle}}{n_{steps}}$$

1.2 The setup menu

For the example problem we assume that the system is starting from an undeformed state. The analysis is divided in to 3 ranges.The purpose of using 3 ranges is to minimize initial transients.

The first range is the Static range when the input speed is 0.00. The second range is dynamic when the input speed increases from 0 r.p.m to 1623 r.p.m. The ramping from minimum speed to maximum speed is controlled by the STARTSPEEDFACTOR parameter. The STARTSPEEDFACTOR for range 1 and range 2 is 0.0. The third step is again dynamic when the input member (Sun gear for this example) maintains a constant speed of $1623rpm$. The STARTSPEEDFACTOR for range 3 is 1.00. The solution method for the Static range is STATIC and that for the dynamic ranges we use the NEWMARK method.

For this problem we run the analysis for about 3000 steps (N_{steps} for each Dynamic range = 3000). For so many steps normally the postprocessing file size goes beyond 2 Gigabytes which may be too large. So generally we do not write the postprocessing file while running dynamic cases (unless it is for less than 100 steps). So do not check the POSTPROCWRITE box. Also most of the results are extracted using Surface gages, FE probes and bearing files. All the other parameters related to the setup menu are given in Table 1.1.

For the dynamic example problem,

$RPM_s = 1623$ r.p.m.

$RPM_R = 0$ r.p.m.

$N_s = 27$.

$N_R = 99$.

N_{steps} for first (Static) range = 1.00

N_{steps} for second (Dynamic) range = 1000

N_{steps} for third (Dynamic) range = 3000

Using the above data and the formulas,

T_{cycle} = 1.742E-3 secs.

Time step (For 100 steps per tooth cycle) = 1.742E-5 secs.

Table 1.1: Setup menu

Item	Description
SEPTOL	3e-3
NPROFDIVS	3
DSPROFSUN	0.2
DSPROFRING	0.2
INITIALTIME	0.0
NRANGES	3
RANGE	1
SOLMETHOD	STATIC
NTIMESTEPS	1
DELTATIME	1.742E-5
STARTSPEEDFACTOR	0.0
STARTTORQUEFACTOR	1.0
ENDTORQUEFACTOR	1.0
RANGE	2
SOLMETHOD	NEWMARK
NTIMESTEPS	1000
DELTATIME	1.742E-5
STARTSPEEDFACTOR	0.0
STARTTORQUEFACTOR	1.0
ENDTORQUEFACTOR	1.0
RANGE	3
SOLMETHOD	NEWMARK
NTIMESTEPS	3000
DELTATIME	1.742E-5
STARTSPEEDFACTOR	1.0
STARTTORQUEFACTOR	1.0
ENDTORQUEFACTOR	1.0
NSTEPSAVE	500
SAVEFILENAME	restper.dat
OUTPUTFILENAME	restout.dat

1.3 Analysis and Results

Before starting an analysis, sensor locations have to be set up to measure stresses and loads in the model. User should place the surface gages, feprobes and load sensors at appropriate locations depending upon the requirement of results. Once the sensors are set up click on the generate model button to check for any errors or warnings. If there are none then click on the STARTANAL button to start the analysis.

The *2DPlanetary* analysis package creates files like PINIONnBRGRES.DAT, SUNBRGRES.DAT, HOUSINGRES.DAT, GAGES.DAT, FEPROBES.DAT, LOADS.DAT etc after the analysis is complete. All these files are created in the working directory. Figure 1.1 shows the plot of maximum principal normal stress for the fillet surface on the sun gear using the data from GAGES.DAT. The information for the Surface gage whose output is shown in Figure 1.1 is described in Table 1.2. Each row in the file GAGES.DAT corresponds to a time instant. The first column in the file contains the value of time. The remaining columns contain the data for the surface gages. There are 4 columns of data for each gage. So as to obtain the plot shown in the figure we have used the data from the first(critical maximum principal normal stress) and the second(critical minimum principal normal stresses) column for Gage no.1.

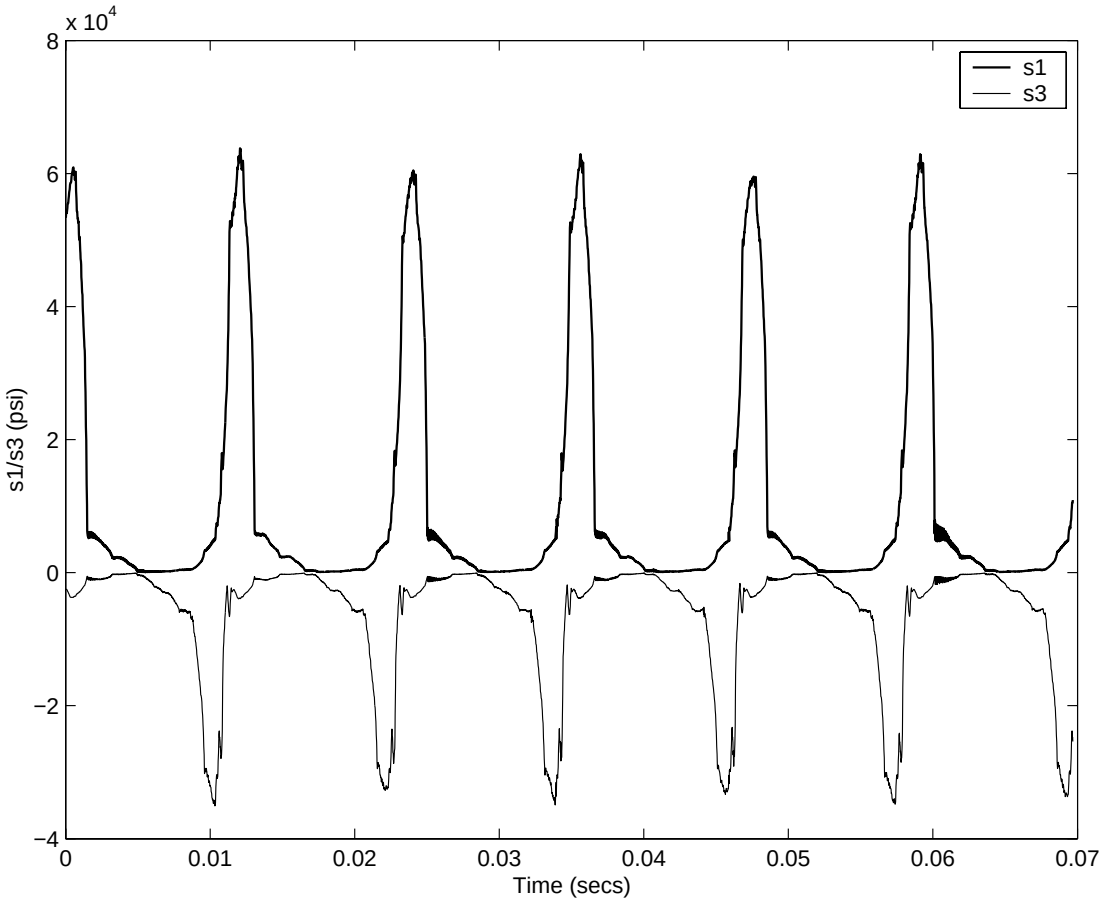

Figure 1.1: Graph showing the dynamic maximum principal normal stresses (s1) and minimum principal normal stresses (s3) against time for the fillet surface of the sun gear, measured by Surfage Gage 1. The results are obtained from the file GAGES.DAT.

Table 1.2: Surface gage data for extracting the plot shown in Figure 1.1

Item	Gage 1
BODY	SUN
SURFACE	FILLET1
TOOTHBEGIN	1
TOOTHEND	1
SPROFBEGIN	0.00
SPROFEND	15.00
NUMSPROF	51
TFACEBEGIN	0.00
TFACEEND	0.00
NUMTFACE	1
DEPTHBEGIN	0.00
DEPTHEND	0.00
NUMDEPTH	1
DISTMIN	0.005
FILENAME	GAGES.DAT

The dynamic analysis should attain a steady state behavior after some time. This can be checked for using the pinion bearing reaction plots as shown in the Figure 1.2. This plot shows the pinion bearing tangential displacement against time. The data for the plot is obtained from the PINION1BRGRES.DAT file. The file contains the results for Pinion1 Bearing. It has one row for each instant of time analyzed. The first column contains the time. The third column will give the tangential displacement for Pinion1. Reaction forces transmitted in the Housing can be checked using the housing bearing reaction plots. A plot of timestep against housing moments is shown in Figure 1.3. Column no.13 in the HOUSINGRES.DAT file gives the moment about the Z-axis for each time instant.

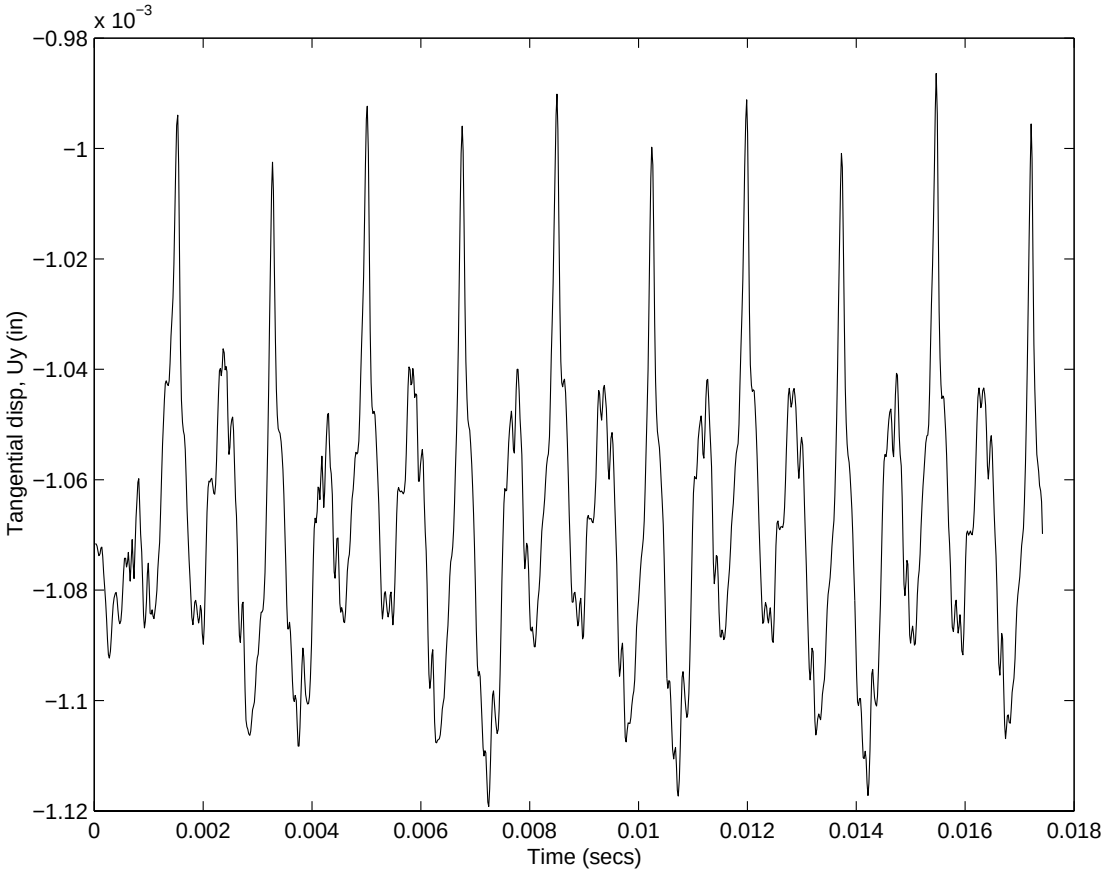

Figure 1.2: Graph showing the pinion bearing tangential displacement against time for dynamic analysis. The tangential displacement at each instant of time is given in Column no.3 of the PINION1BRGRES.DAT file.

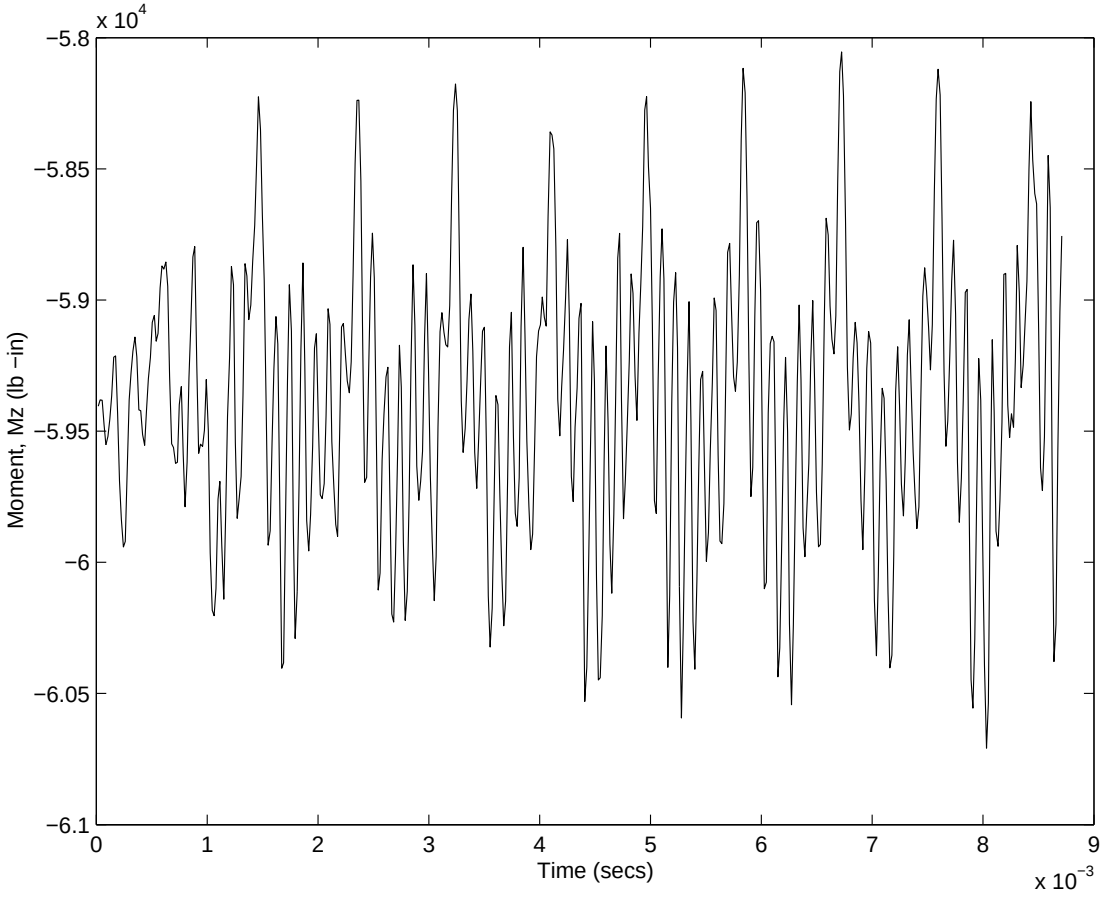

Figure 1.3: Graph showing the housing moments against time for dynamic analysis. The moment about the Z-axis for each time instant is given in column no.13 of the HOUSINGRES.DAT file

1.3.1 Calculating the Dynamic load factor

A graph of timestep against dynamic loads obtained from the file LOADS.DAT is shown in Figure 1.4. The LOADS.DAT file has one row for each instant of time. The first column contains the time. Each subsequent column contains the reading for one load sensor. Table 1.3 shows the data for a load sensor so as to obtain the plot shown in Figure 1.4. So as to obtain the plot of static loads against time a STATIC analysis is performed on the same planetary gear set. Figure 1.5 shows a plot of static load against time using the TOOTHLOAD command. The TOOTHLOAD data used to extract this plot is given in Table 1.4. Using the static and dynamic load values you can calculate the dynamic load factor, a term very commonly used in the gear industry to predict dynamic stresses from static values.

$$\text{Dynamic Load Factor} \quad = \quad \frac{\text{Dynamic Height}}{\text{Static Height}} \tag{1.1}$$

For the present example, the `Dynamic Load Factor` $= \frac{3514.50}{2909.23} = 1.208$

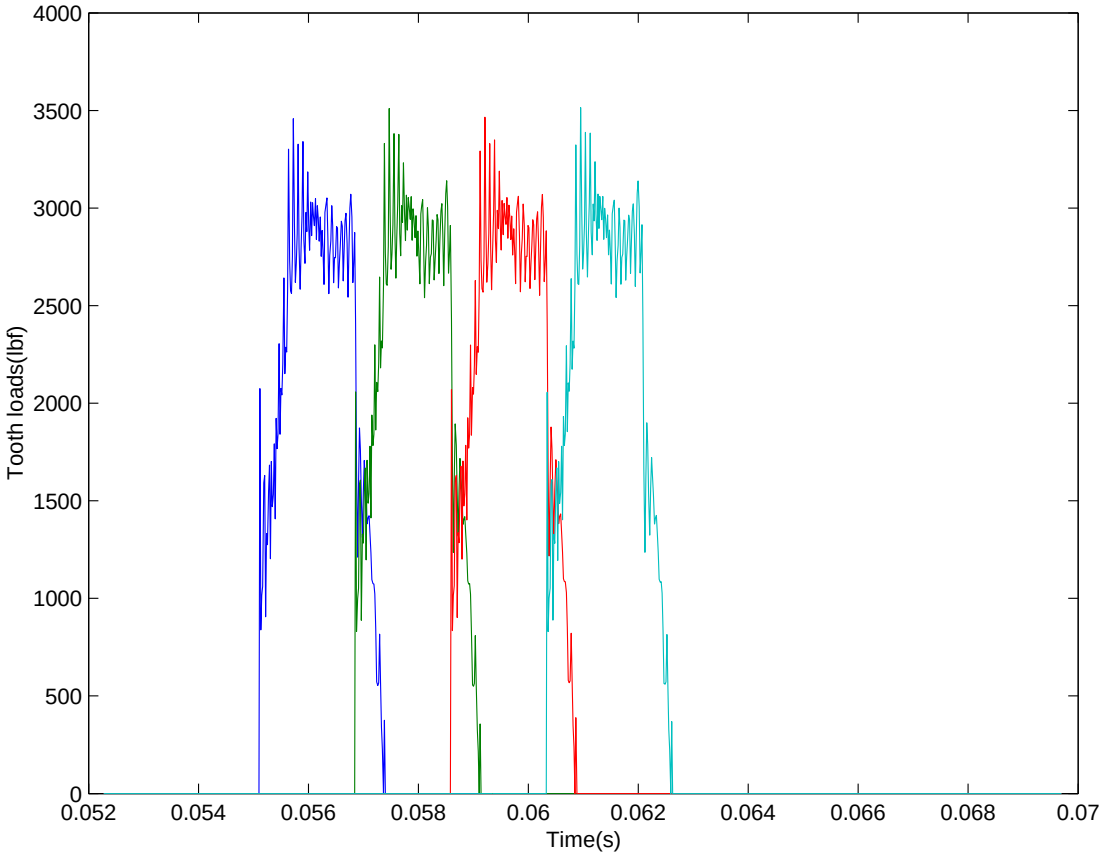

Figure 1.4: Graph showing the dynamic tooth load against time. The plot is obtained using the load values from column nos.6, 10, 11 and 12 from the LOADS.DAT file.

Table 1.3: Load sensor data for extracting the plot shown in Figure 1.4

Item	Description
NLOADSENSORS	11
LOADSENSOR	5
SURFPAIR	PINION1_SURFACE1_SUN_SURFACE1
MEMBER	SUN
TOOTH	1
FILENAME	LOADS.DAT

Table 1.4: Tooth load data for extracting the plot shown in Figure 1.5

Item	Description
SURFACEPAIR	PINION1_SURFACE1_SUN_SURFACE1
MEMBER	SUN
TOOTHBEGIN	1
TOOTHEND	1
BEGINSTEP	1
ENDSTEP	11

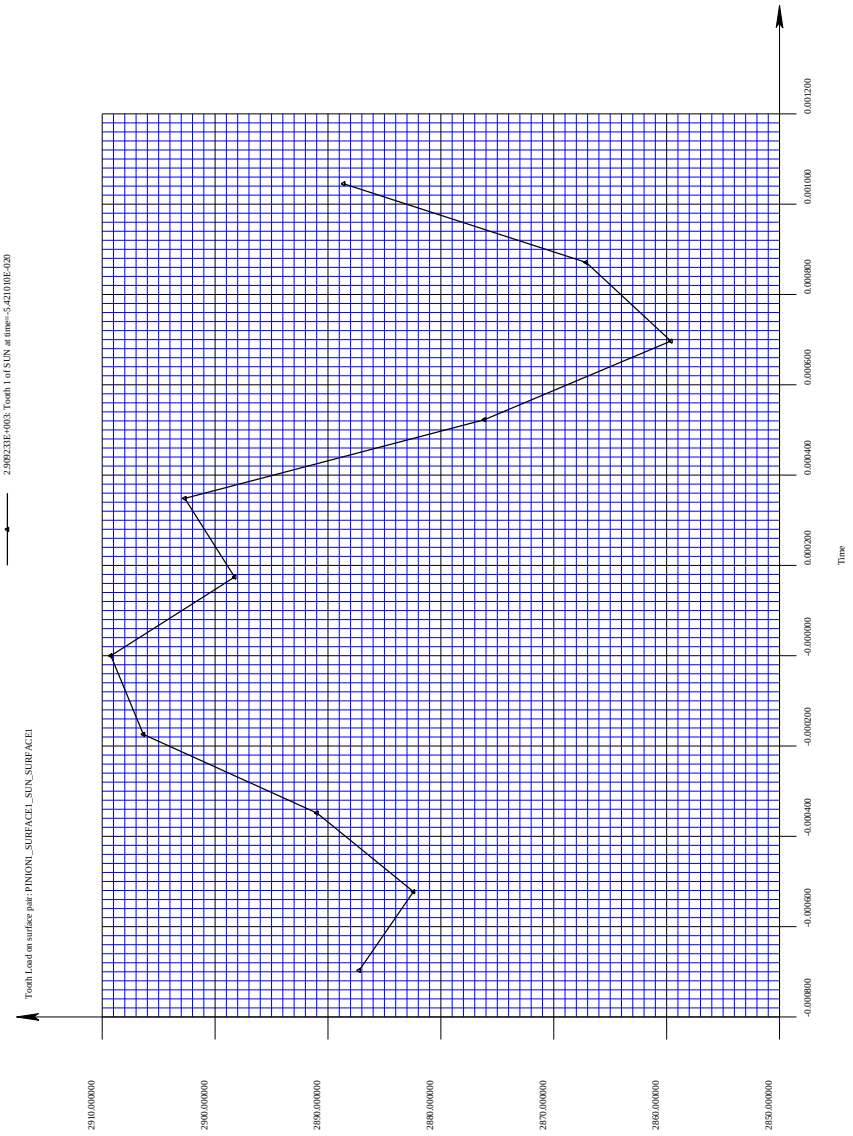

Figure 1.5: Graph showing the static tooth load against time using the TOOTHLOAD command.

Chapter 2

Effect of Pin position errors on the planet load distribution

The position of the pinion pin or the bearing can be moved by a small amount from the ideal position as shown in Figure 2.1. This deflection of the pinion pin or the bearing from its ideal position is called the pinion pin position error. The pin position error affects the load distribution on individual planets in a planetary system. Following study demonstrates the ability of the *2DPlanetary* software package to analyse this effect.

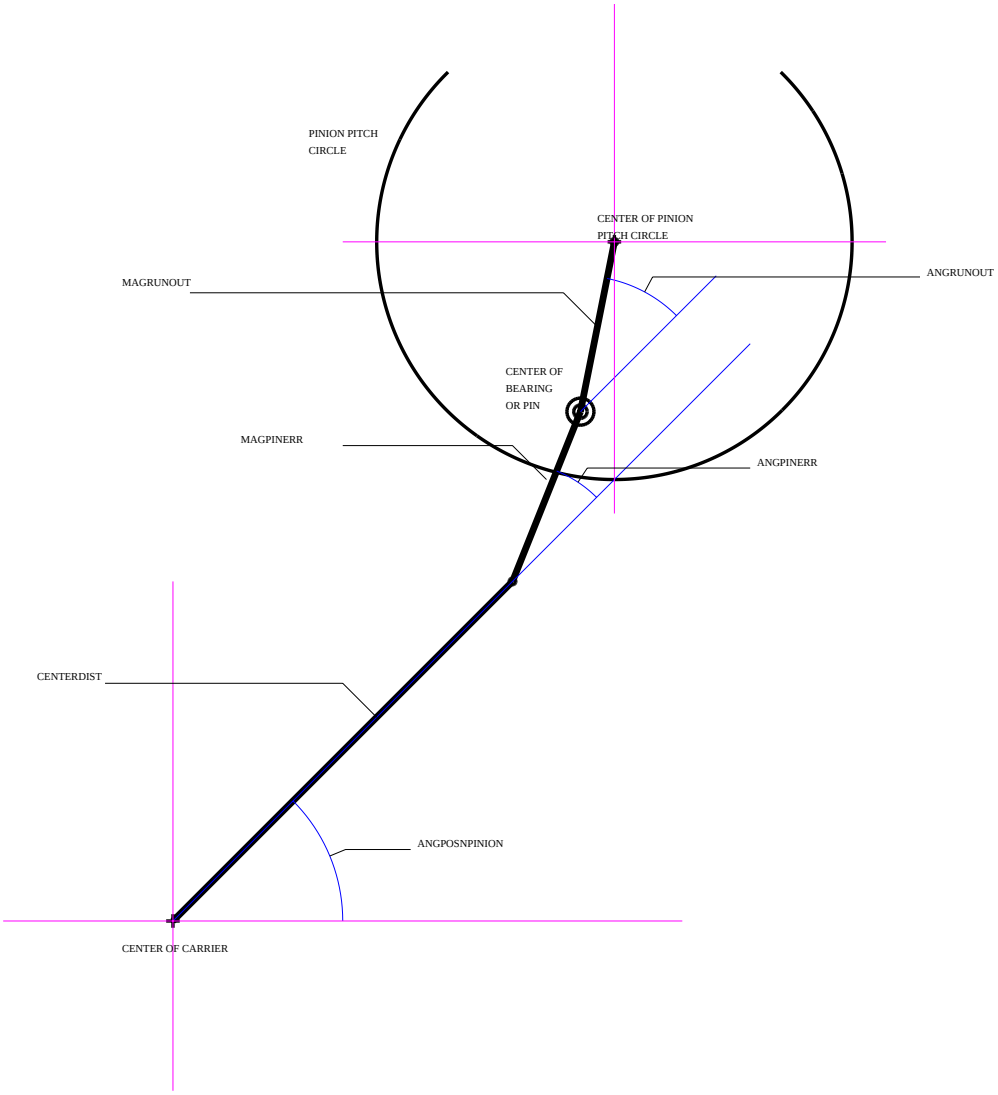

Figure 2.1: The pinion assembly errors.

2.1 Effect of pin position errors on a 4 pinion planetary system

Load the file `nopinposnerr4pins.ses` located in the Working directory. This a 4 pinion planetary system model with no pinion pin position errors. A static run for one mesh cycle is conducted.

The deformation and reaction forces generated in each bearing are saved in data files during analysis. These data files are named after the bearings. For example, the file `PINION1BRGRES.DAT` contains the results for the pinion1 bearing, `SUNBRGRES.DAT` contains results for the sun bearing. And `CARRIERBRGRES.DAT` contains the results for the carrier bearing. Each data file has one row for each instant of time analyzed. The first column contains the time. The next 6 columns contain the six components of bearing deformation, u_x, u_y, u_z, θ_x, θ_y, and θ_z. The last 6 columns contain the 6 components of bearing reaction, F_x, F_y, F_z, M_x, M_y, and M_z.

For the present case we look at the tangential component of the force in each pinion bearing. The pinion bearing reference frame is oriented with its Y-axis along the tangential direction. F_y is in the 9th column of the bearing results file. Figure 2.2 shows the load distribution on each pinion at each time instant. From the plot we can conclude that the load distribution on each planet for the system with no pin position errors is more or less equal.

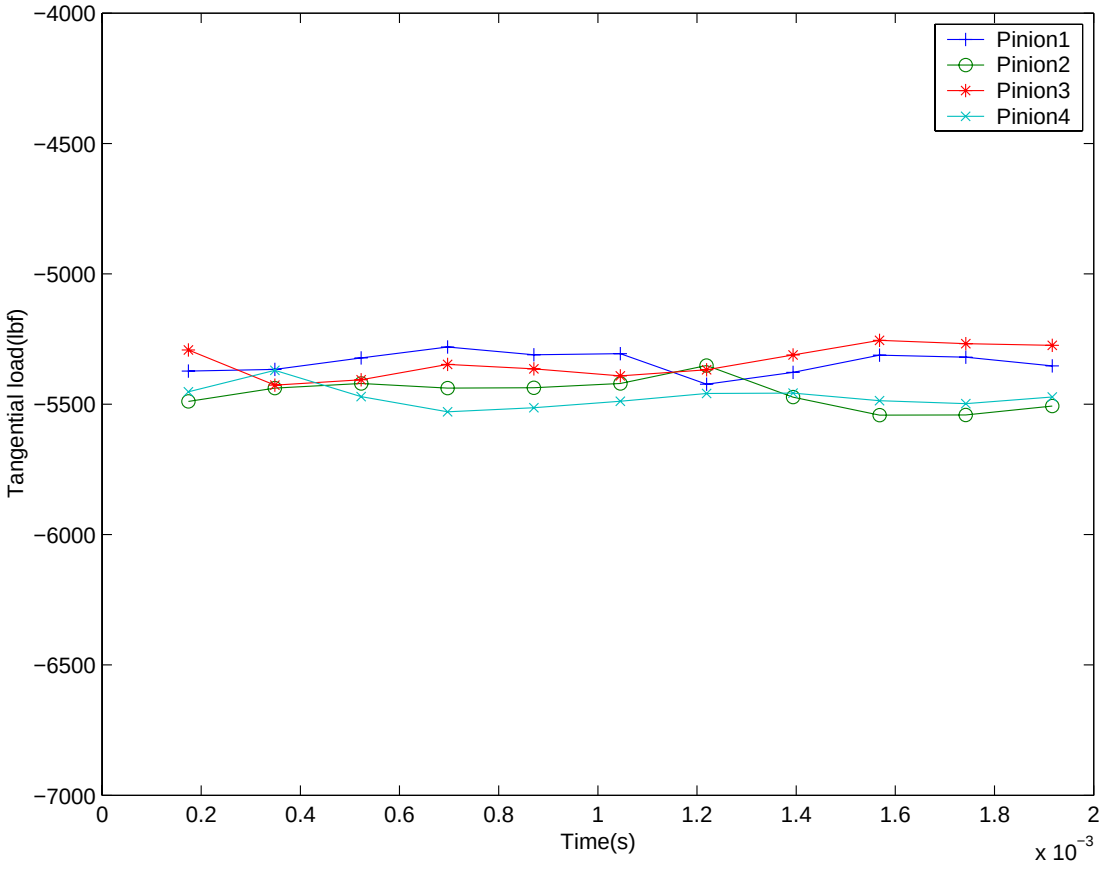

Figure 2.2: Load distribution on each pinion for a 4 pinion planetary system with no pin position errors.

Load the file `pinposnerr4pins.ses` located in the Working directory. A pin position error of $0.001in$ is applied on Pinion no.2 in the tangential direction. The data for the PINPOSNERR menu is given in Table 2.1. A static run for one mesh cycle is conducted.

Table 2.1: Pin position error menu

Item	Description
NUMPINIONS	4
PINIONNO	2
MAGNITUDE	0.001
ANGLE	90

Figure 2.3 shows the plot of load distribution against time for each pinion. As can be seen from the plot the load shared by Pinion 2 is more than that shared by the other pinions. The load on Pinion 2 increases from $5.3514 \times 10^3 lbf$ to $5.89994 \times 10^3 lbf$ after the position error is applied.

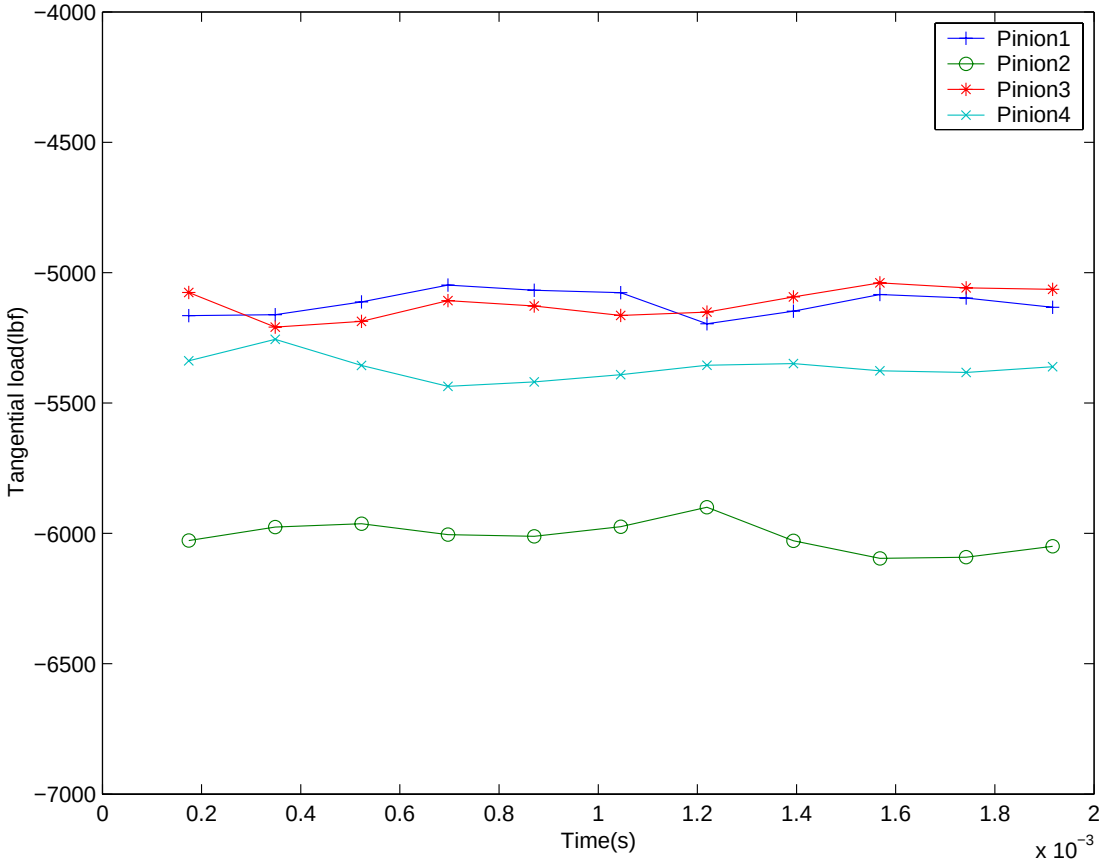

Figure 2.3: Load distribution on each pinion for a 4 pinion planetary system with pin position error applied on Pinion 2.

Load the file `pinposnerrflsun4pins.ses` located in the Working directory. The effect of a floating sun gear on the load distribution on pinions with pin position error on Pinion 2 is demonstrated in this example. A static run for one mesh cycle is conducted.

Figure 2.4 shows the plot of load distribution against time for each pinion when the sun is floating. This plot shows that when the sun gear is floating (not attached to the axis) the Pinions 2 and 4 share approximately equal loads. The tangential load on Pinion 2 decreases from 5.8994×10^3 to 5.6200×10^3.

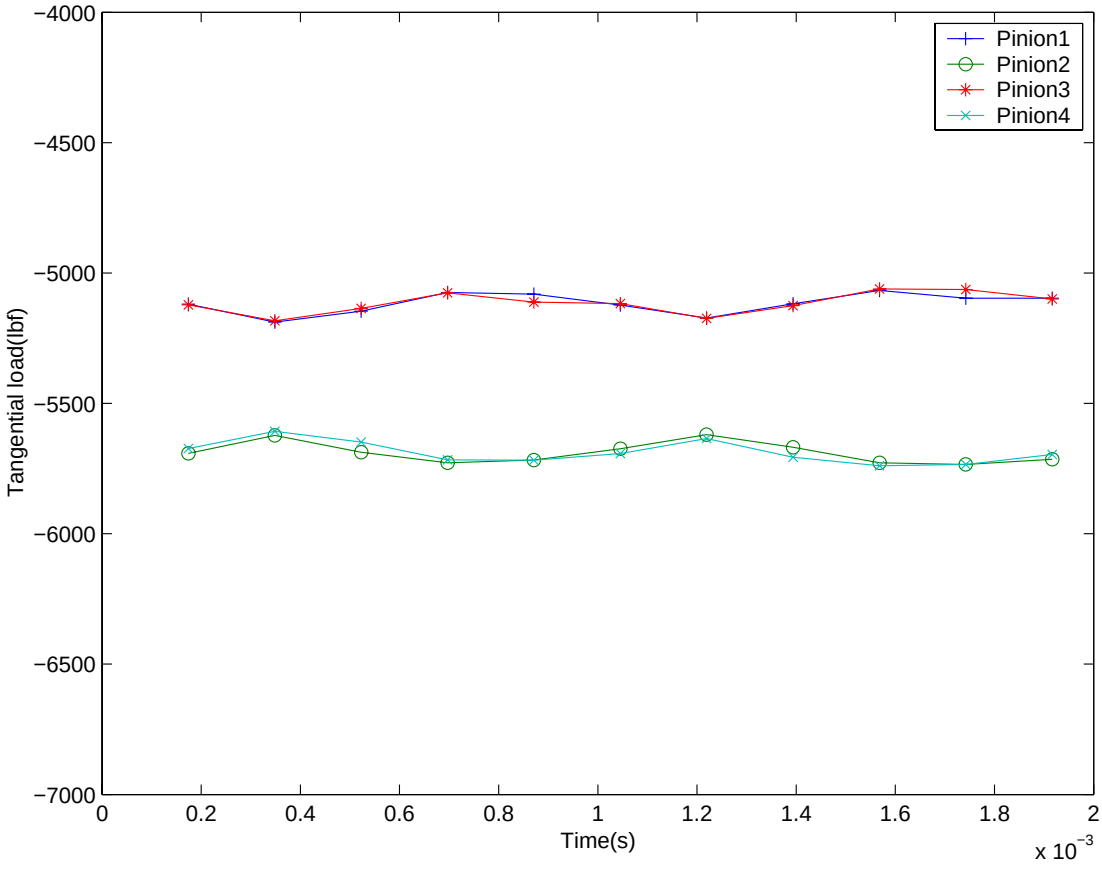

Figure 2.4: Load distribution on each pinion for a floating sun, 4 pinion planetary system with pin position error applied on Pinion 2.

A similar observation was made when instead of having a floating sun gear, the carrier is made floating (`pinposnerrflcarr4pins.ses`). Figure 2.5 shows the plot of load distribution against time for each pinion when the carrier is floating.

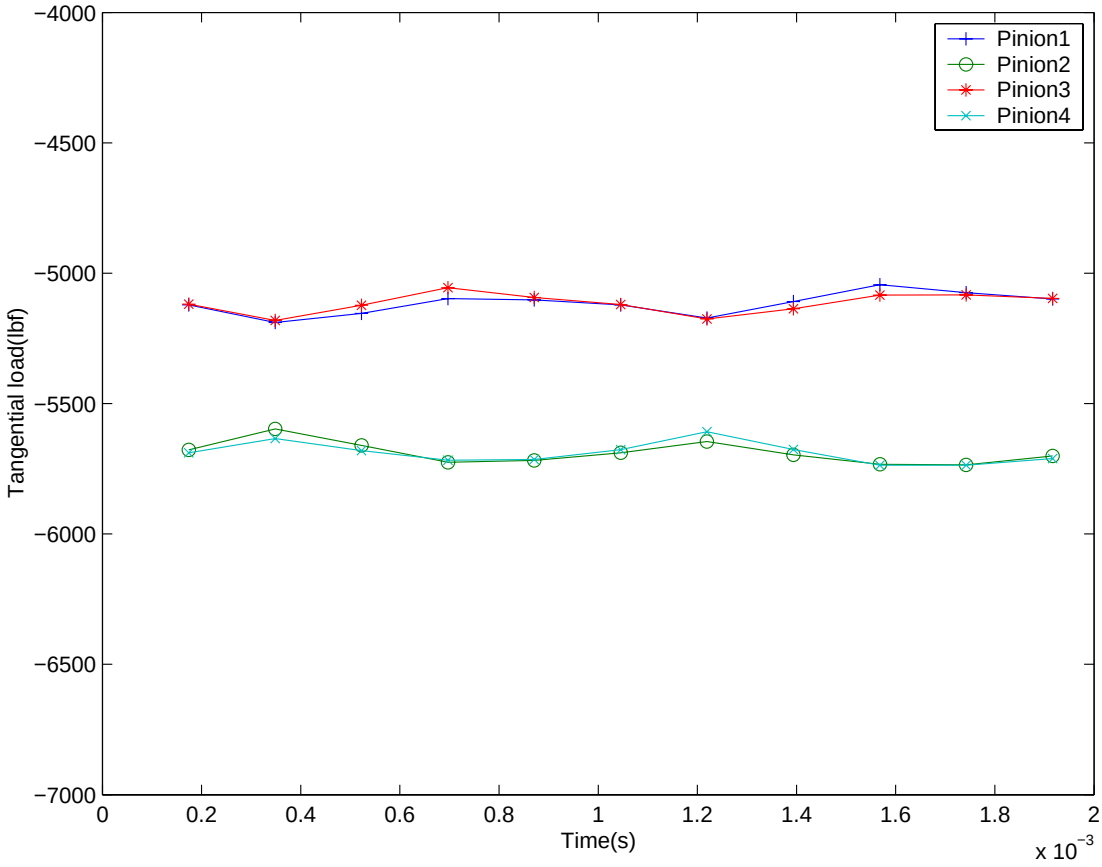

Figure 2.5: Load distribution on each pinion for a floating carrier, 4 pinion planetary system with pin position error applied on Pinion 2.

Figure 2.6 shows the plot of load distribution against time for each pinion when both the sun and carrier are floating (`pinposnerrflsunflcarr4pins.ses`). The load in this case is equally shared by the opposite pinions. Table 2.2 summarizes the load values in each case for the 4 pinion system.

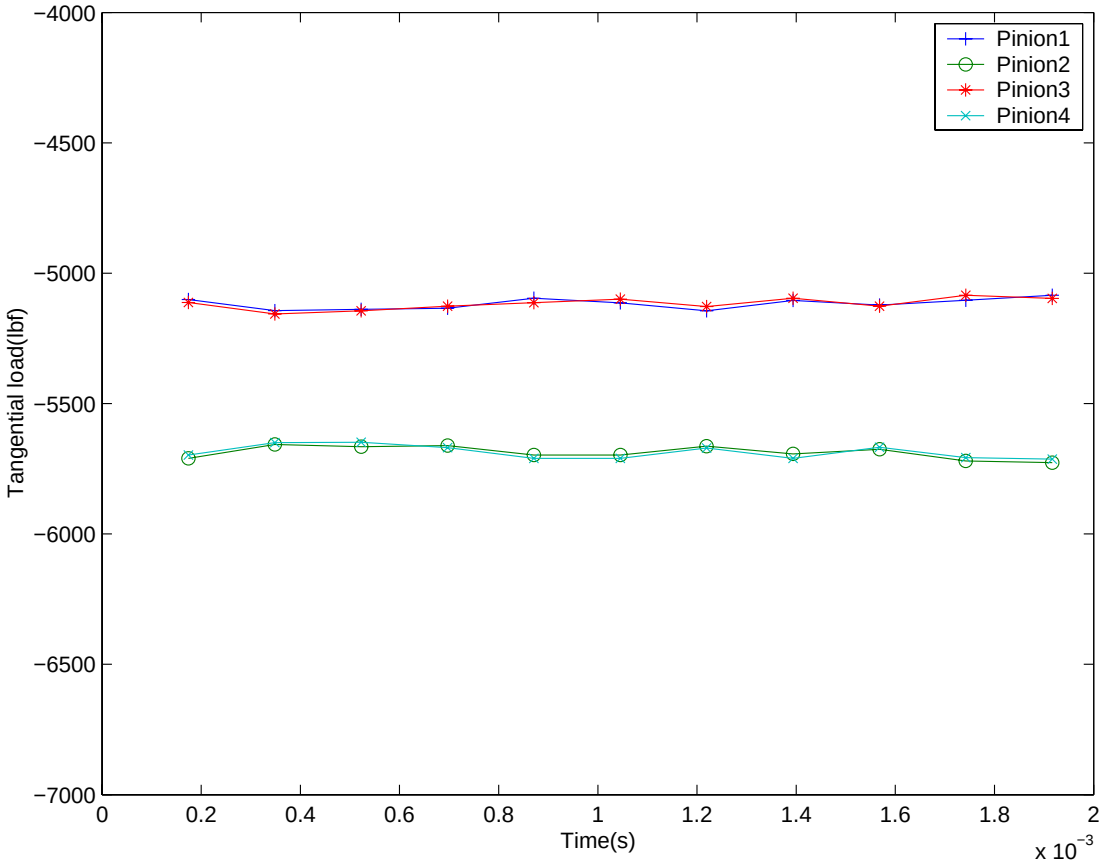

Figure 2.6: Load distribution on each pinion for a floating sun and carrier, 4 pinion planetary system with pin position error applied on Pinion 2.

Table 2.2: Load distribution values for a 4 pinion planetary system

Planetary model	Pinion 1(lbf)	Pinion 2(lbf)	Pinion 3(lbf)	Pinion 4(lbf)
No pin position error	5.2804×10^3	5.3514×10^3	5.2553×10^3	5.3703×10^3
Pin position error at Pinion 2	5.0478×10^3	5.8994×10^3	5.0393×10^3	5.2560×10^3
With a floating sun gear	5.0668×10^3	5.6200×10^3	5.0613×10^3	5.6073×10^3
With a floating carrier	5.0440×10^3	5.5973×10^3	5.0556×10^3	5.6081×10^3
With floating sun and carrier	5.0850×10^3	5.6566×10^3	5.0843×10^3	5.6484×10^3

2.2 Effect of pin position errors on a 3 pinion planetary system

Load the file `nopinposnerr3pins.ses` located in the Working directory. This a 3 pinion planetary system model with no pinion pin position errors. Figure 2.7 shows the load distribution on each pinion at each time instant. The load sharing by each pinion is more or less equal.

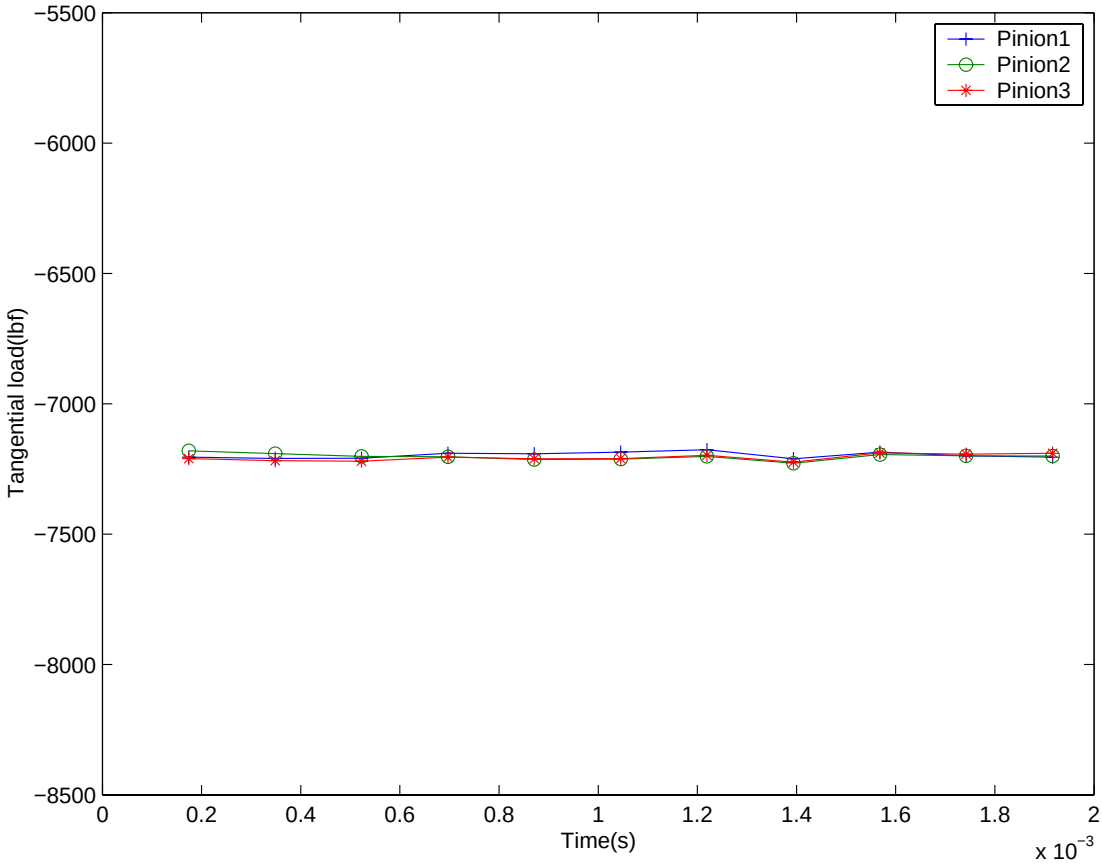

Figure 2.7: Load distribution on each pinion for a 3 pinion planetary system with no pin position errors.

Load the file `pinposnerr3pins.ses` located in the Working directory. So as to study the effect of pin position errors on a 3 pinion planetary system we apply a position error of $0.001in$ at Pinion 2 in the tangential direction. A static run of one mesh cycle is performed on this model. Figure 2.8 shows the plot of load distribution against time for each pinion. As can be seen from the plot the load shared by Pinion 2 is more than that shared by the other pinions. The load on Pinion 2 increases from $7.1801 \times 10^3 lbf$ to $7.7756 \times 10^3 lbf$ after the position error is applied.

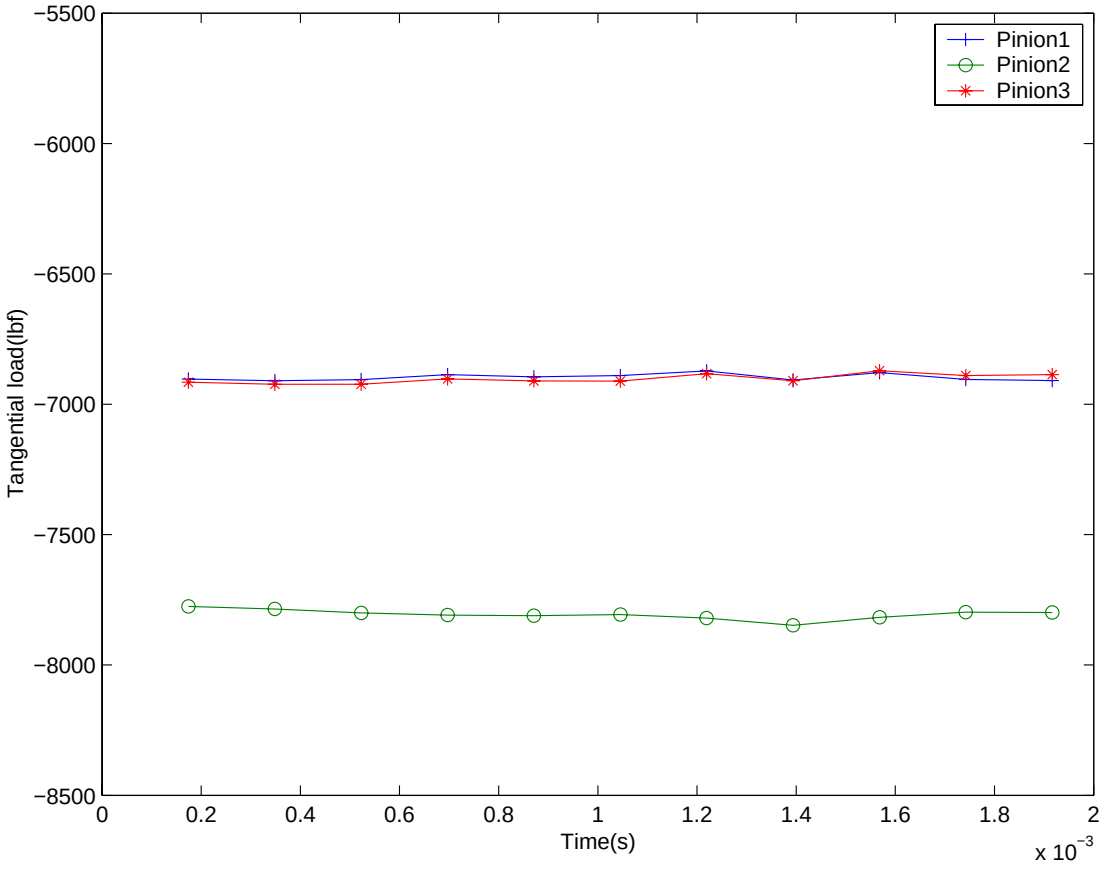

Figure 2.8: Load distribution on each pinion for a 3 pinion planetary system with pin position error applied on Pinion 2.

Figure 2.9 shows the plot of load distribution against time for each pinion when the sun is floating (`pinposnerrflsun3pins.ses`). This plot shows that when the sun gear is floating (not attached to the axis) all the Pinions share approximately equal loads inspite of one of the pinions having a pin-position error. The tangential load on Pinion 2 decreases from 7.7756×10^3 to 7.1895×10^3.

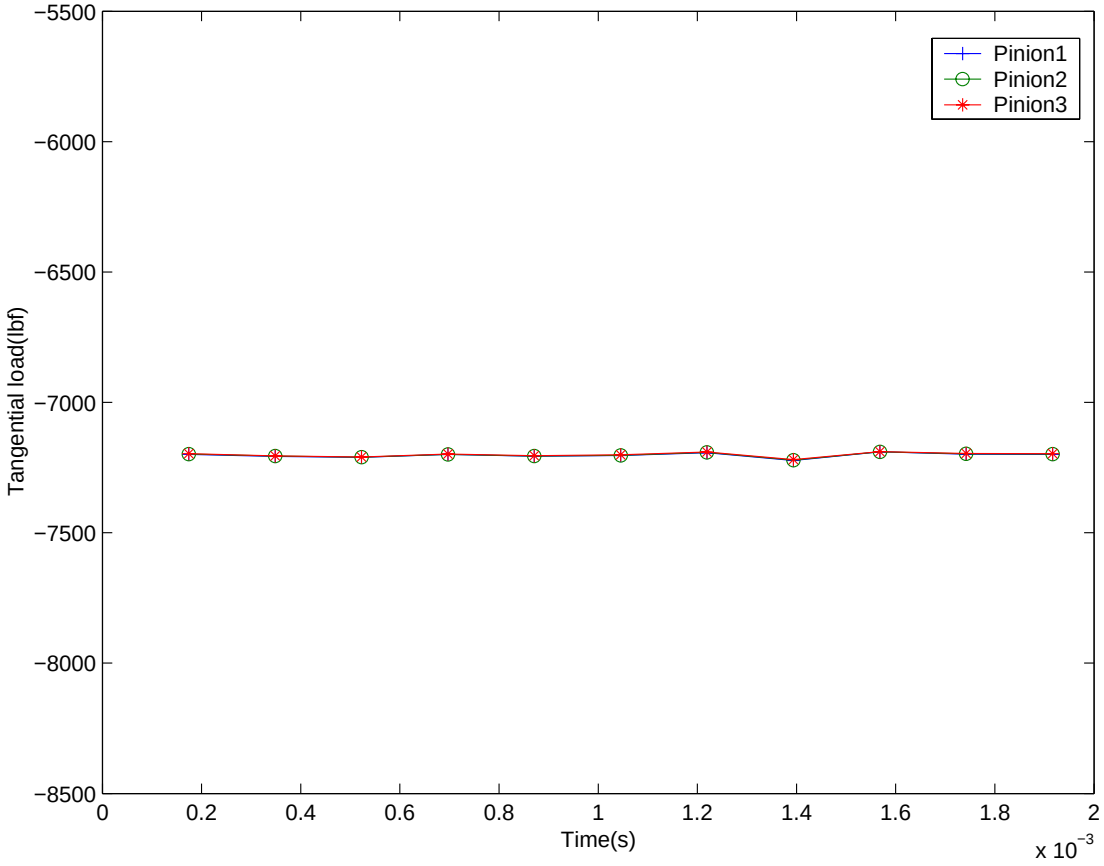

Figure 2.9: Load distribution on each pinion for a floating sun, 3 pinion planetary system with pin position error applied on Pinion 2.

A similar observation was made when instead of having a floating sun gear, the carrier is made floating (`pinposnerrflcarr3pins.ses`). Figure 2.10 shows the plot of load distribution against time for each pinion when the carrier is floating.

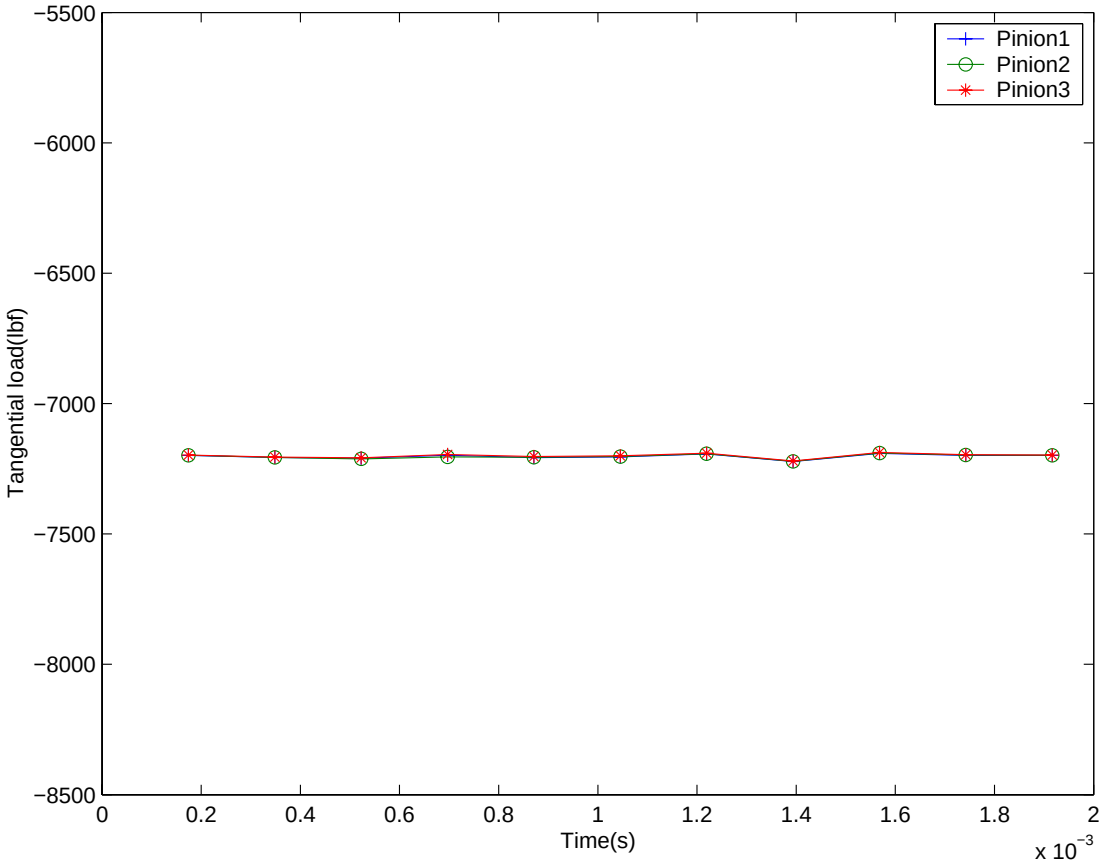

Figure 2.10: Load distribution on each pinion for a floating carrier, 3 pinion planetary system with pin position error applied on Pinion 2.

Figure 2.11 shows the plot of load distribution against time for each pinion when both the sun and carrier are floating (`pinposnerrflsunflcarr3pins.ses`). The load in this case is equally shared by all the pinions. Table 2.3 summarizes the load values in each case for the 3 pinion system.

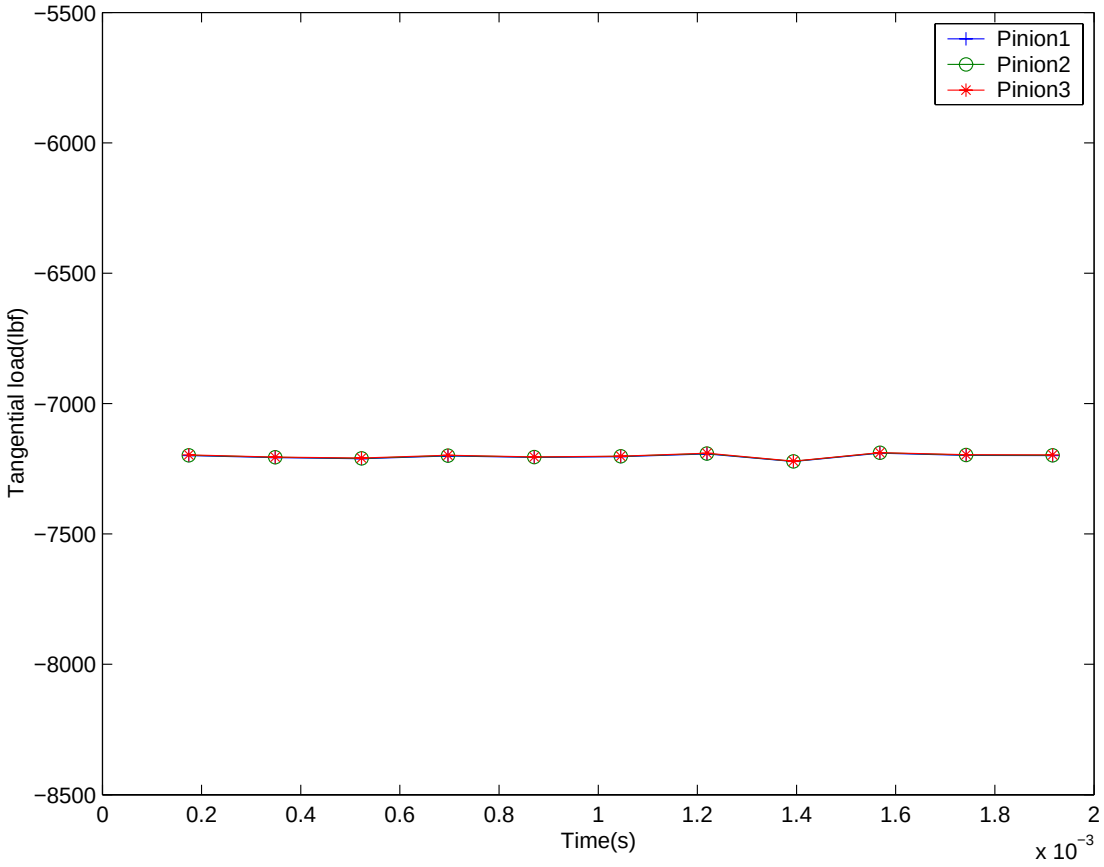

Figure 2.11: Load distribution on each pinion for a floating sun and carrier, 3 pinion planetary system with pin position error applied on Pinion 2.

Table 2.3: Load distribution values for a 3 pinion planetary system

Planetary model	Pinion 1(lbf)	Pinion 2(lbf)	Pinion 3(lbf)
No pin position error	7.1761×10^3	7.1801×10^3	7.1884×10^3
Pin position error at Pinion 2	6.8719×10^3	7.7756×10^3	6.8717×10^3
With a floating sun gear	7.1896×10^3	7.1895×10^3	7.1888×10^3
With a floating carrier	7.1910×10^3	7.1896×10^3	7.1873×10^3
With floating sun and carrier	7.1905×10^3	7.1892×10^3	7.1881×10^3

2.3 Effect of pin position errors on a 5 pinion planetary system

Load the file `nopinposnerr5pins.ses` located in the Working directory. This a 5 pinion planetary system model with no pinion pin position errors. Figure 2.12 shows the load distribution on each pinion at each time instant. The load sharing by each pinion is more or less equal.

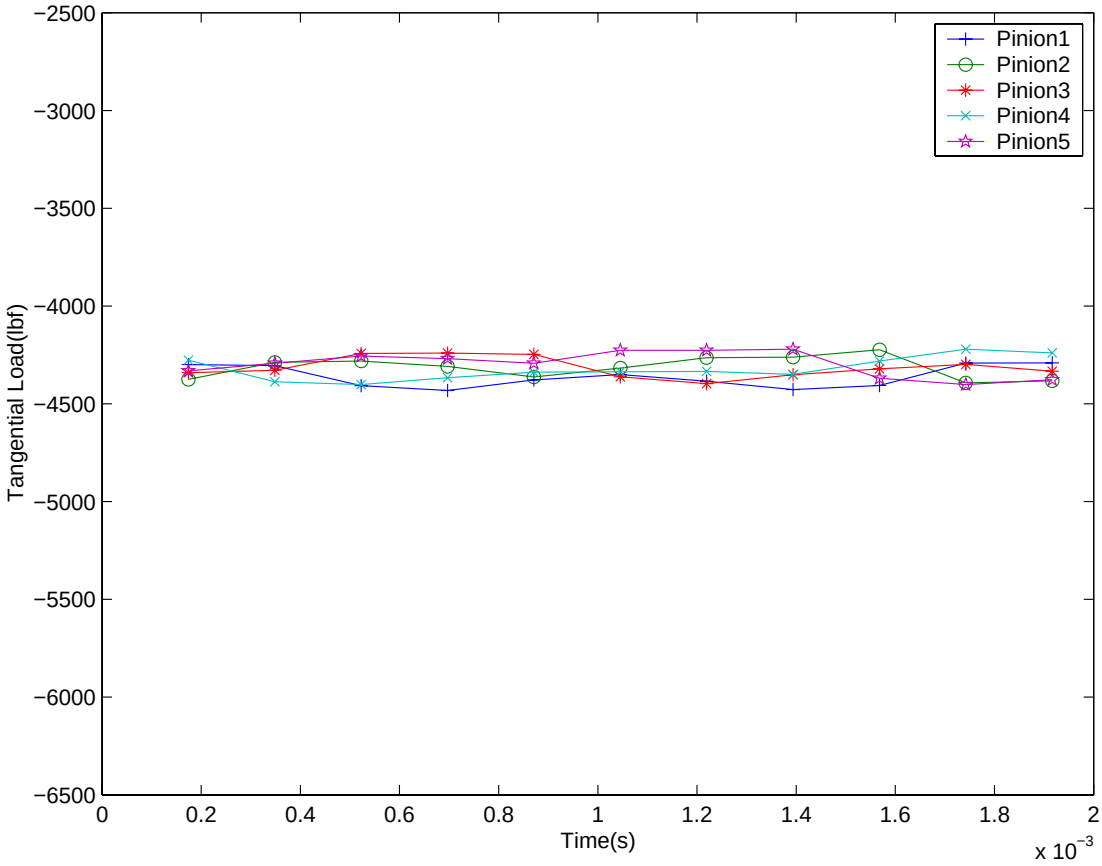

Figure 2.12: Load distribution on each pinion for a 5 pinion planetary system with no pin position errors.

Load the file `pinposnerr5pins.ses` located in the Working directory. So as to study the effect of pin position errors on a 5 pinion planetary system we apply a position error of $0.001in$ at Pinion 2 in the tangential direction. A static run of one mesh cycle is performed on this model. Figure 2.13 shows the plot of load distribution against time for each pinion. As can be seen from the plot the load shared by Pinion 2 is more than that shared by the other pinions. The load on Pinion 2 increases from $4.2233 \times 10^3 lbf$ to $4.9191 \times 10^3 lbf$ after the position error is applied.

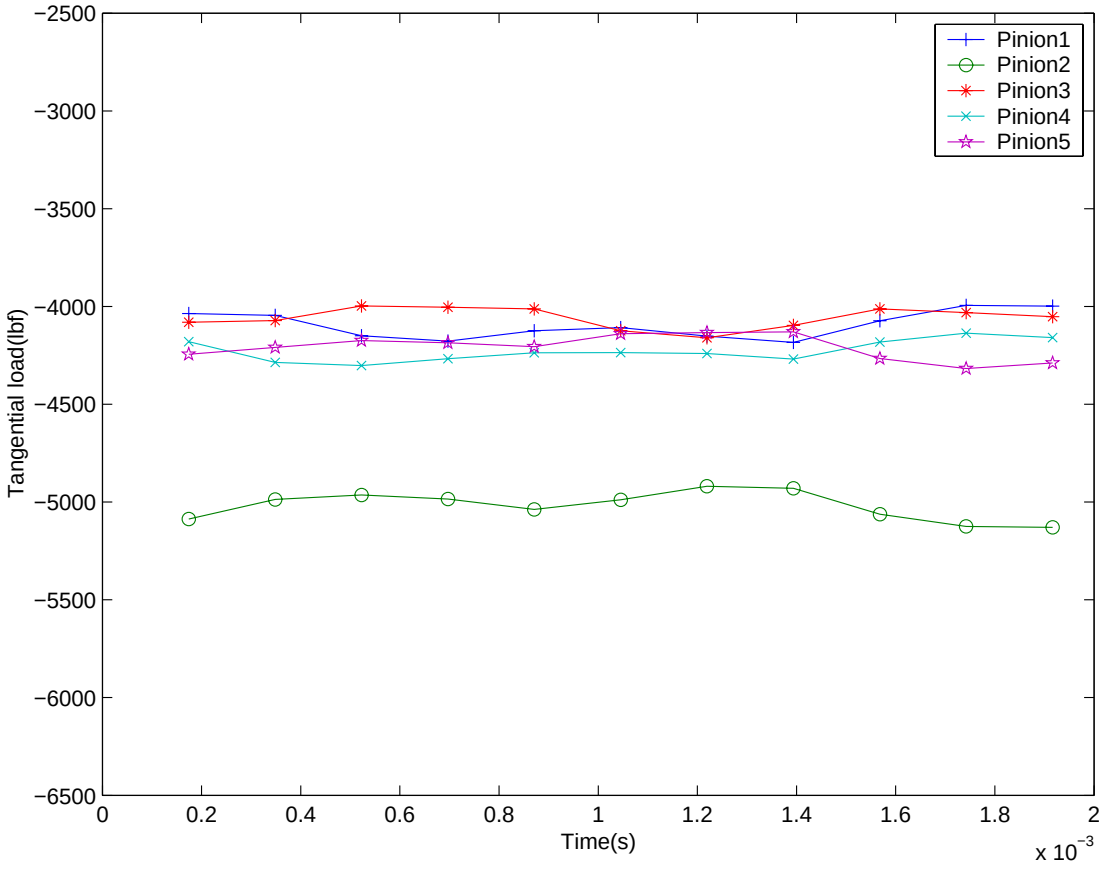

Figure 2.13: Load distribution on each pinion for a 5 pinion planetary system with pin position error applied on Pinion 2.

Figure 2.14 shows the plot of load distribution against time for each pinion when the sun is floating (`pinposnerrflsun5pins.ses`). This plot shows that when the sun gear is floating (not attached to the axis) the load on Pinion 2 decreases from $4.9191 \times 10^3 lbf$ to $4.6255 \times 10^3 lbf$. Load shared by Pinions 1 and 3 is about the same. Also load shared by Pinions 4 and 5 is aproximately equal.

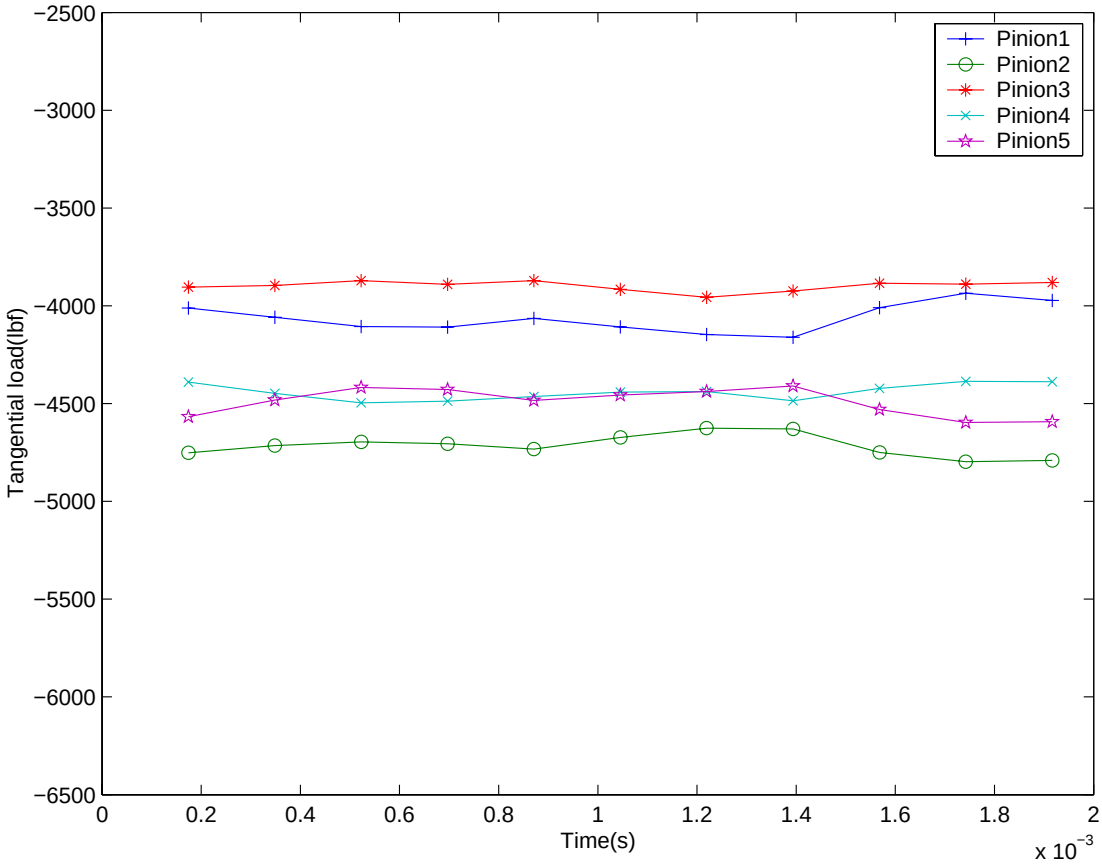

Figure 2.14: Load distribution on each pinion for a floating sun, 5 pinion planetary system with pin position error applied on Pinion 2.

A similar observation was made when instead of having a floating sun gear, the carrier is made floating (`pinposnerrflcarr5pins.ses`). Figure 2.15 shows the plot of load distribution against time for each pinion when the carrier is floating.

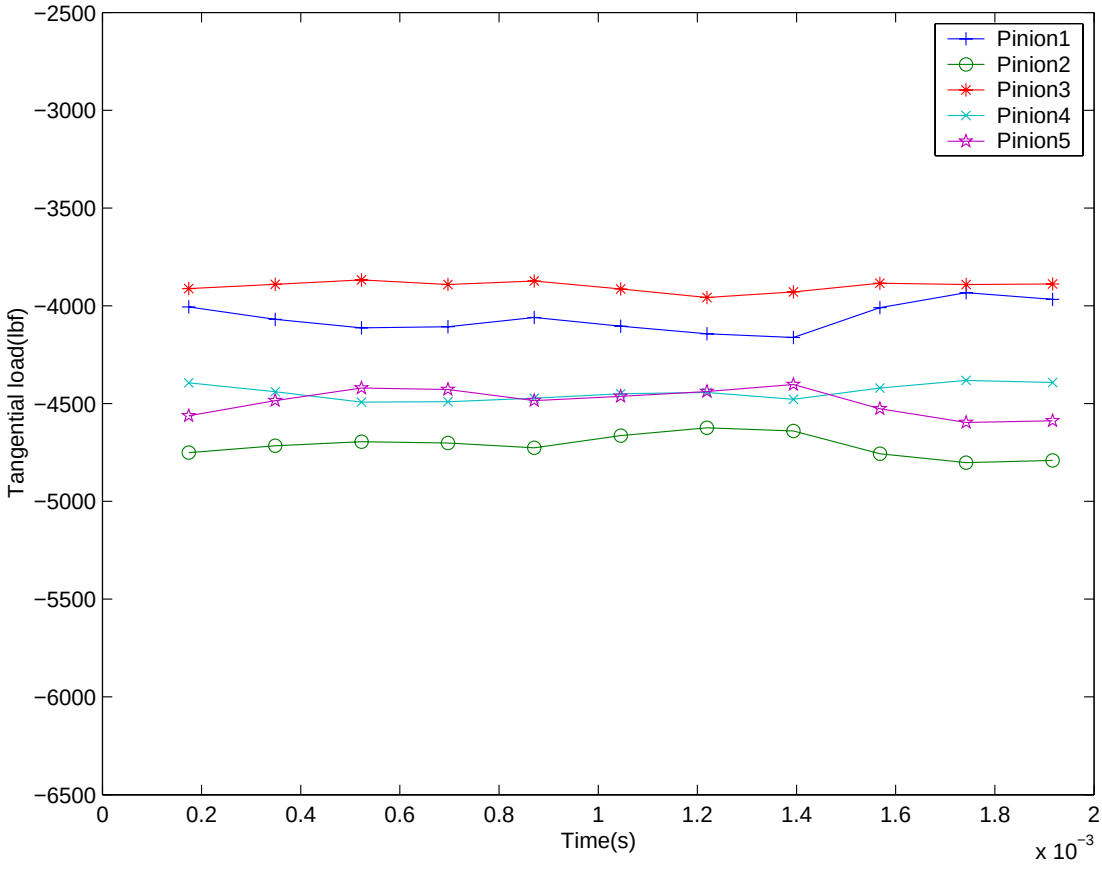

Figure 2.15: Load distribution on each pinion for a floating carrier, 5 pinion planetary system with pin position error applied on Pinion 2.

Figure 2.16 shows the plot of load distribution against time for each pinion when both the sun and carrier are floating (`pinposnerrflsunflcarr5pins.ses`). The load on Pinion 2 decreases further although this change is not very significant. Table 2.4 summarizes the load values in each case for the 3 pinion system.

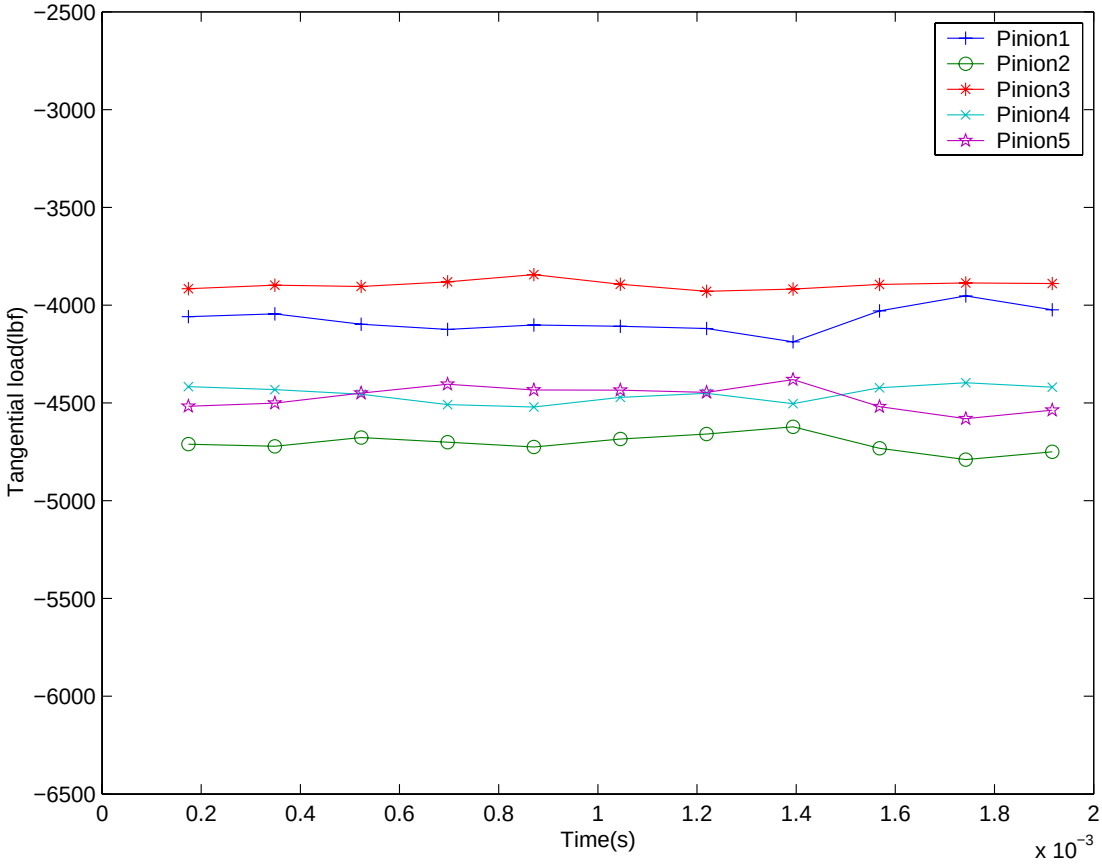

Figure 2.16: Load distribution on each pinion for a floating sun and carrier, 5 pinion planetary system with pin position error applied on Pinion 2.

Table 2.4: Load distribution values for a 5 pinion planetary system

Planetary model	Pinion 1(lbf)	Pinion 2(lbf)	Pinion 3(lbf)	Pinion 4(lbf)	Pinion 5(lbf)
No pin position error	4.2912×10^3	4.2233×10^3	4.2409×10^3	4.2208×10^3	4.2211×10^3
Pin position error at Pinion 2	3.9943×10^3	4.9191×10^3	3.9976×10^3	4.1365×10^3	4.1295×10^3
With a floating sun gear	3.9360×10^3	4.6255×10^3	3.8709×10^3	4.3862×10^3	4.4098×10^3
With a floating carrier	3.9331×10^3	4.6243×10^3	3.8675×10^3	4.3816×10^3	4.4020×10^3
With floating sun and carrier	3.9525×10^3	4.6224×10^3	3.8444×10^3	4.3972×10^3	4.3805×10^3

2.4 Summary

Pinion pin position errors affect the load sharing amongst the planets. The pinion at which the position error is applied carries more load than the other pinions in the planetary system. The load on the pinion where the position error is applied can be reduced by floating the sun or the carrier or both. For a 4 planet system the load shared by the opposite pinions is equal when the sun or the carrier is floating. For a 3 planet system the load shared by the pinions is insensitive to pin-position errors when the sun or the carrier is made floating.

Chapter 3

Comparison of Experimental results and results obtained from Calyx

Krantz [2] has published stress measurements made by strain gages on the ring gear and sun gear of a spur planetary gear set from a helicopter transmission. It was decided to build a model of the same gear set using Multyx and compute root stresses using Calyx. Figure 3.1 shows the model that was generated. The carrier is rigid and is supported by flexible bearings. There are four pinions. Each pinion is connected to the carrier through a bearing. The sun gear is also supported by bearings. The inner diameter of the sun gear is rigid and the inner diameters of the pinions are flexible. The outer diameter of the ring gear is also flexible. The ring gear is supported through splines on its outer diameter. Contact constraints are enforced between the two sides of each spline tooth and the housing. One side of the spline tooth has a clearance that is based on the amount of radial movement allowed to the actual ring gear. Many different ways of constraining the ring gear were attempted, but it was determined that this method was the most realistic, and it gave the best ring gear stress results. The gear set was run for 600 time steps. Figure 3.2 shows the loads acting on the sun gear at this position, and the contours of maximum principal normal stress. Figure 3.3 shows the loads acting on the ring gear and the contours of maximum principal normal stress in the ring gear and a pinion. It is interesting to note how the ring gear shows significant root stress even on teeth that are not in contact, due to the rim bending effect. The pinion also shows this effect, but to a lesser extent. Figures 3.4 and 3.5 show the maximum and minimum principal normal stress variation, respectively, in the entire planetary system. Figure 3.6 is a close up of the minimum principal normal stress variation near one of the splines on the ring gear's outer diameter. Figures 3.7 through 3.14 show the published strain gage results and the stresses predicted by calyx at the strain gage locations as a function of time. The gages are mounted on the loaded and unloaded sides of the ring gear and sun gear teeth. The agreement between the experiment and numerical prediction is remarkable.

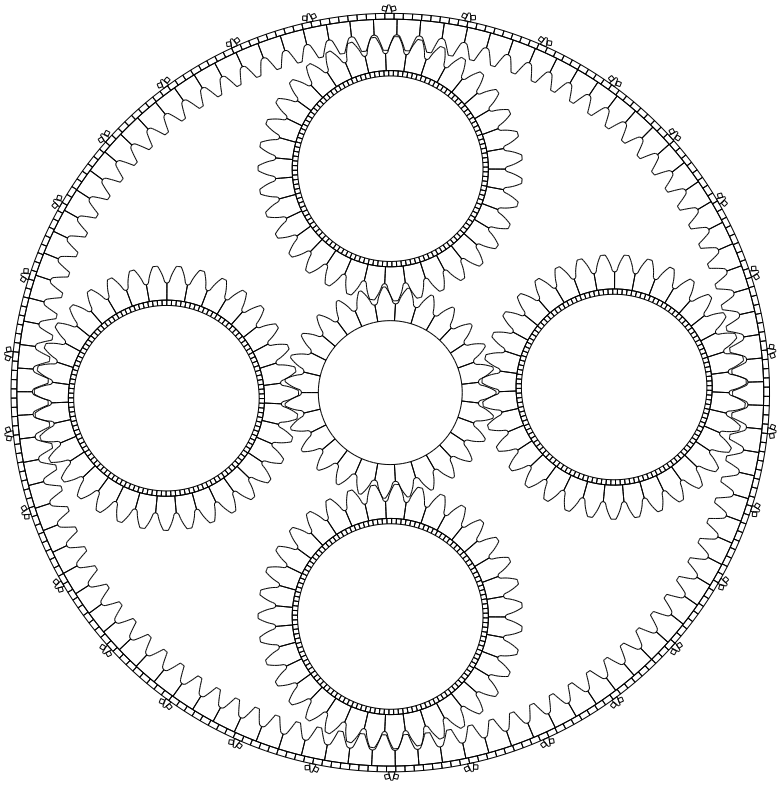

Figure 3.1: Planetary gear set model created through Multyx for comparing results.

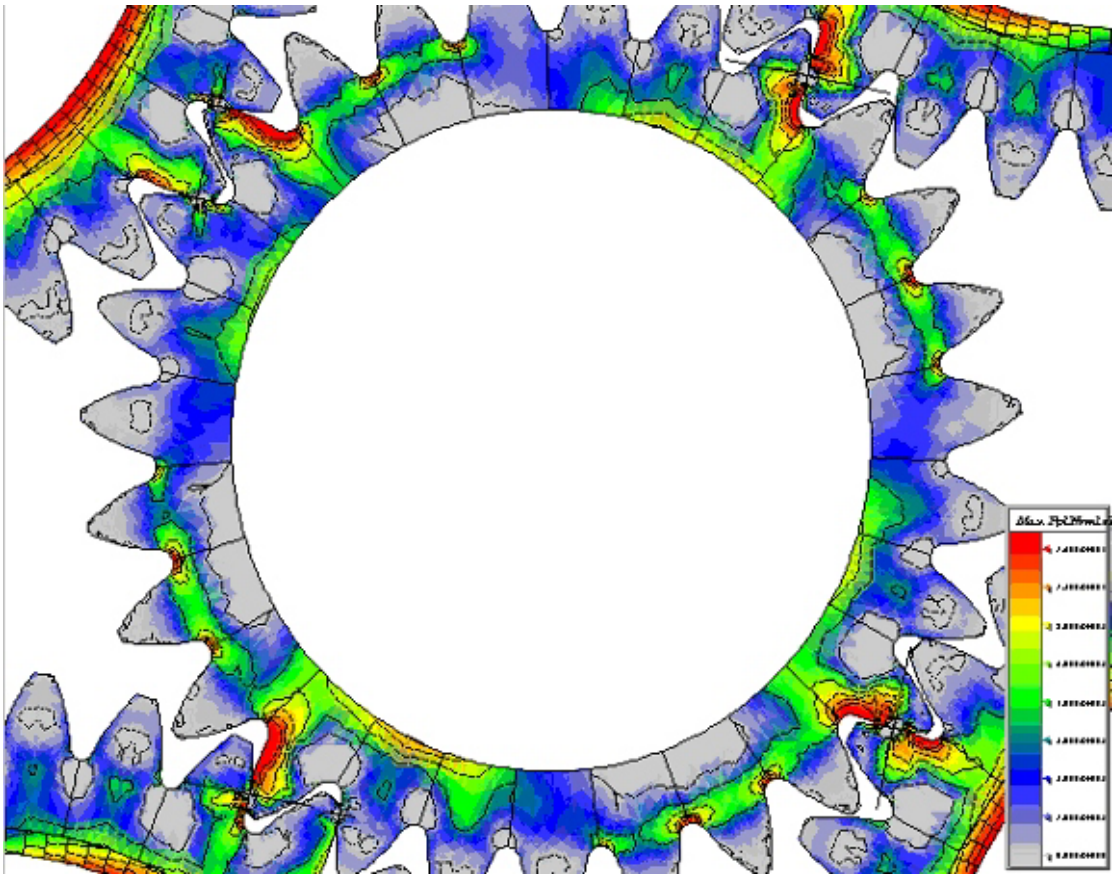

Figure 3.2: Contours of maximum principal normal stress in the sun gear.

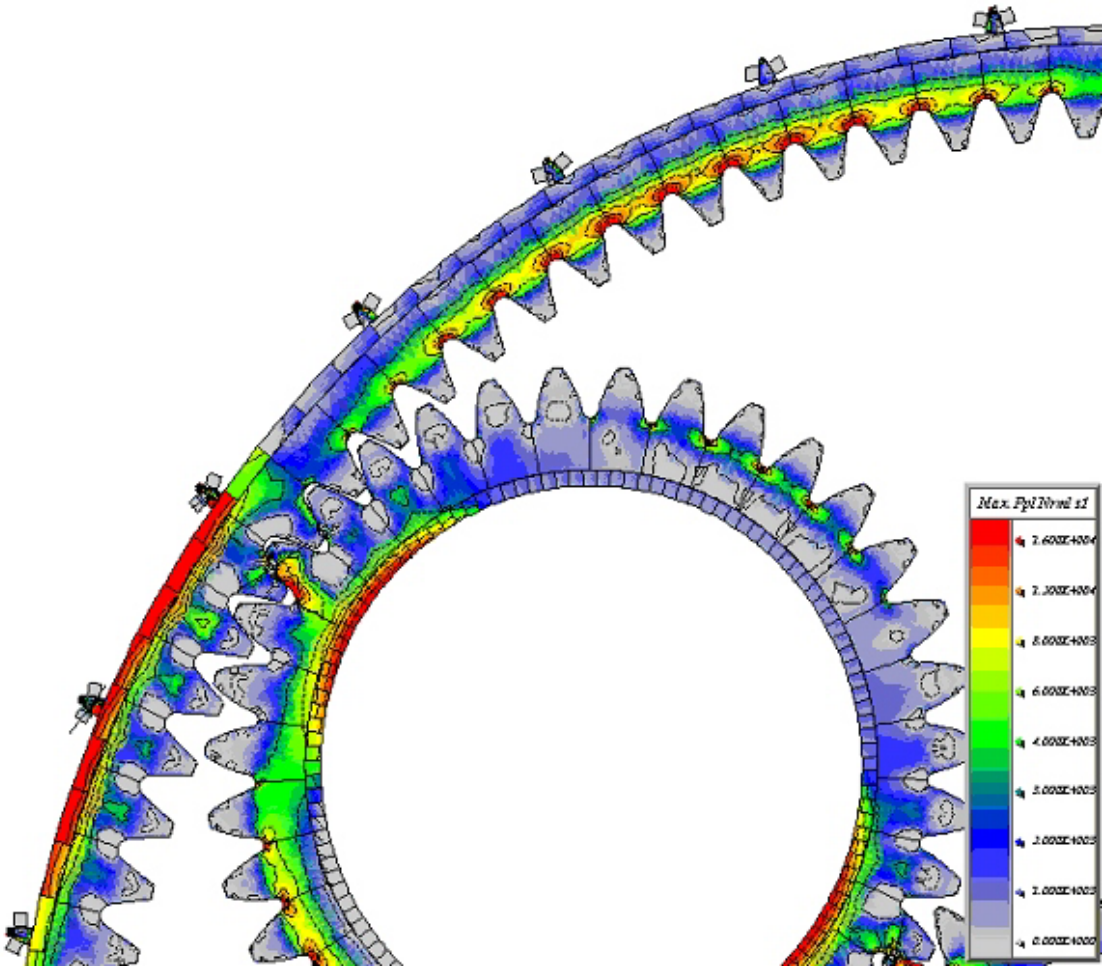

Figure 3.3: Contours of maximum principal normal stress in the ring gear and the pinion.

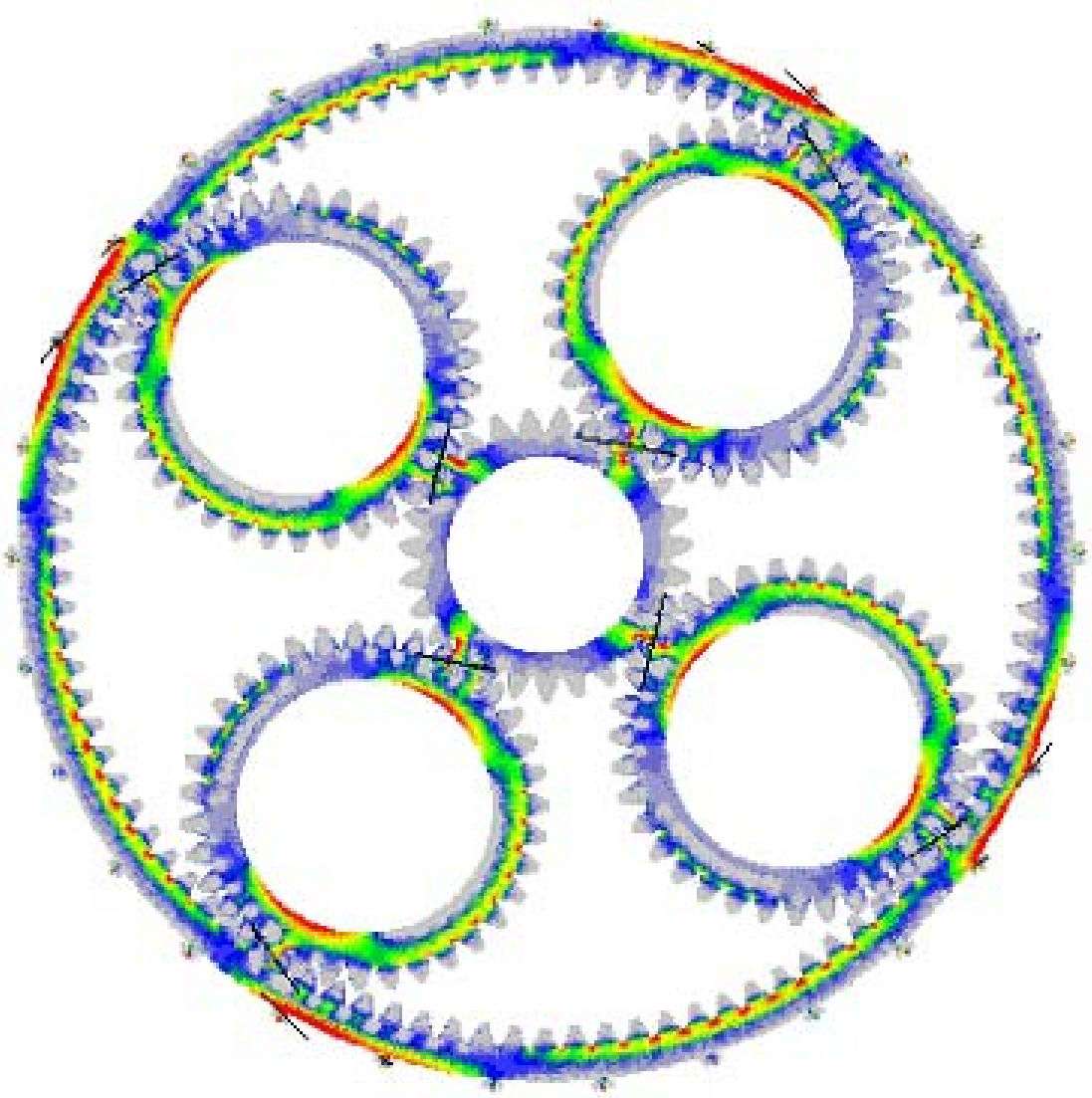

Figure 3.4: Variation of maximum principal normal stress in the planetary gear system.

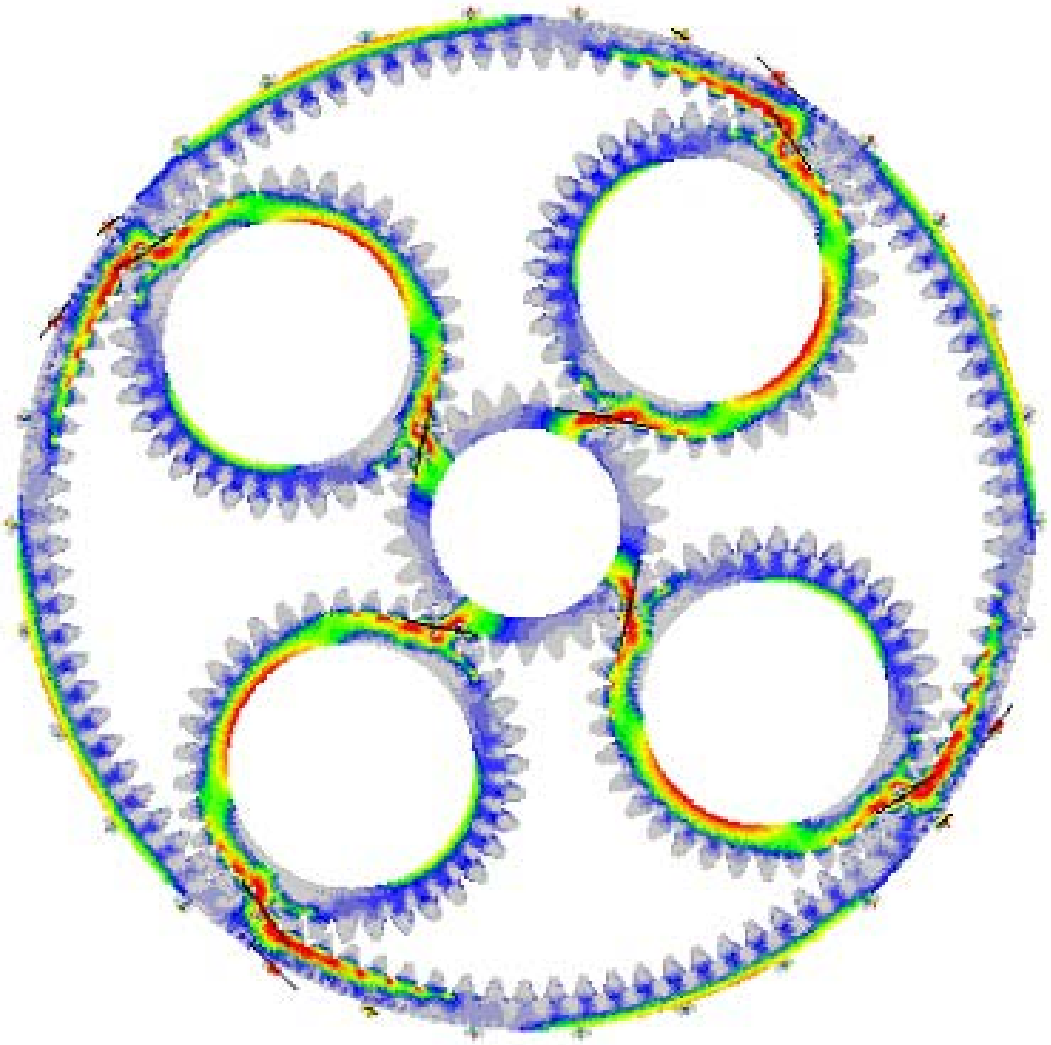

Figure 3.5: Variation of minimum principal normal stress in the planetary gear system.

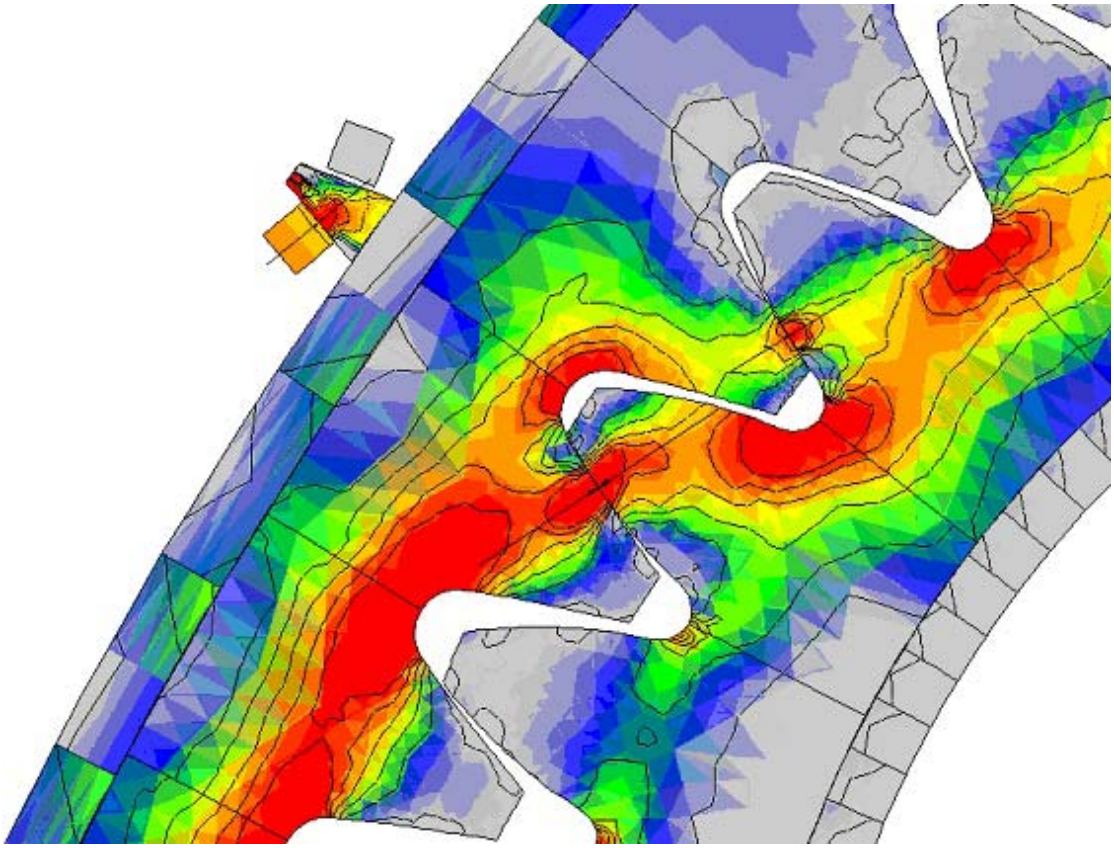

Figure 3.6: Closeup of the minimum principal normal stress variation near one of the splines on the ring gear's outer diameter.

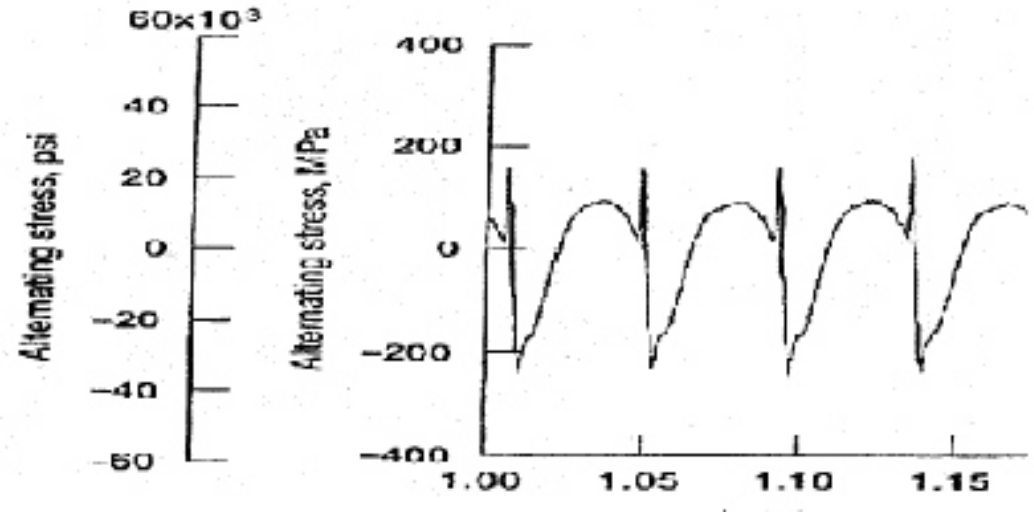

Figure 3.7: Experimental results for stress obtained from strain gages mounted in the fillet on the loaded side of the ring gear tooth. Experimental data is from Krantz [2].



Figure 3.8: Computational predictions of fillet stress on the loaded side of the ring gear tooth.

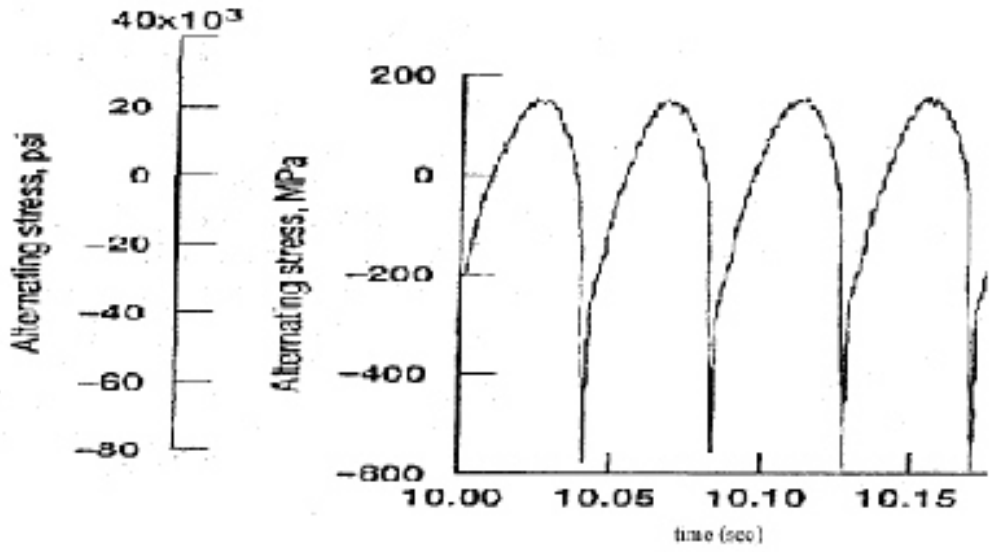

Figure 3.9: Experimental results for stress obtained from strain gages mounted in the fillet on the unloaded side of the ring gear tooth. Experimental data is from Krantz [2]



Figure 3.10: Computational predictions of fillet stress on the unloaded side of the ring gear tooth.

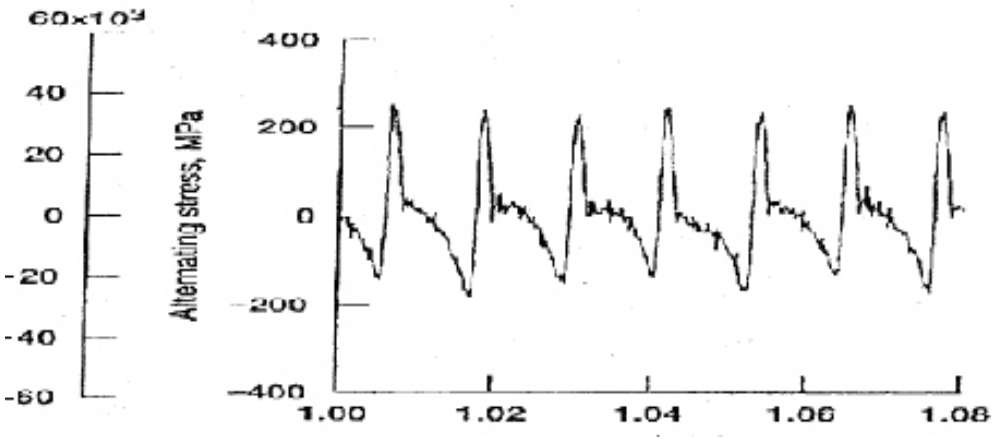

Figure 3.11: Experimental results for stress obtained from strain gages mounted in the fillet on the loaded side of the sun gear tooth. Experimental data is from Krantz [2].

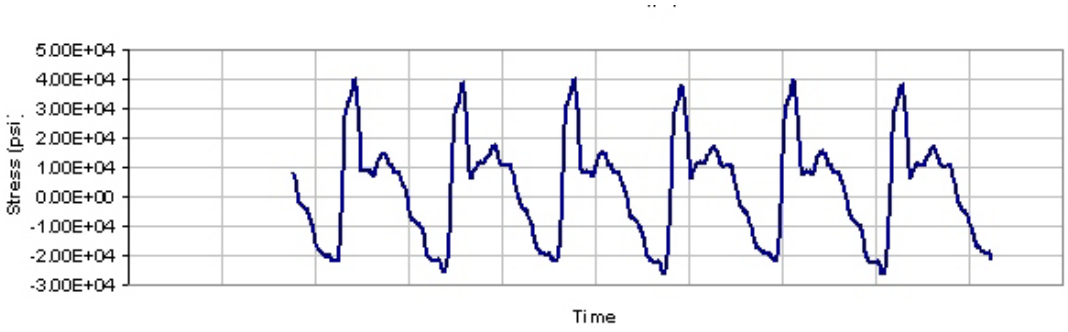

Figure 3.12: Computational predictions of fillet stress on the loaded side of the sun gear tooth.

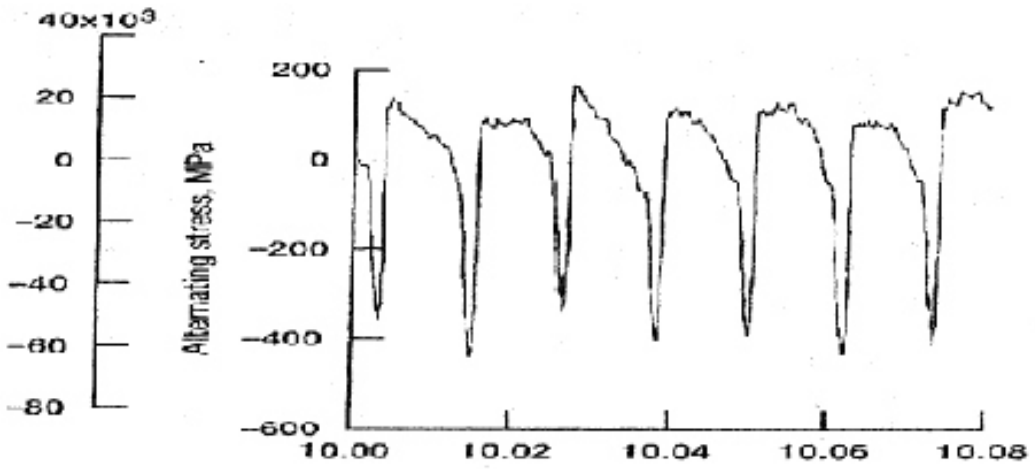

Figure 3.13: Experimental results for stress obtained from strain gages mounted in the fillet on the unloaded side of the ring gear tooth. Experimental data is from Krantz [2].

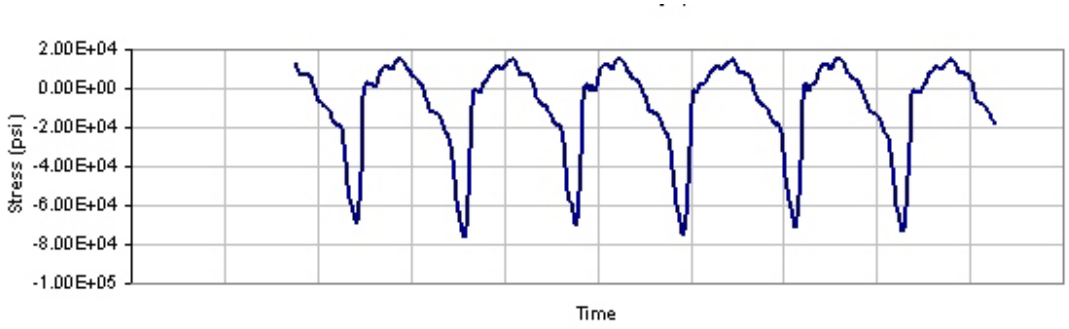

Figure 3.14: Computational predictions of fillet stress on the unloaded side of the ring gear tooth.

Bibliography

[1] *Planetary Gear Train Ring Gear and Support Structure Investigation*, Mark Valco, Ph.D. Dissertation, Cleveland State University, 1992.

[2] *Gear Tooth Stress Measurements of Two Helicopter Planetary Stages*, Krantz, T. L., NASA Technical Memorandum 105651, AVSCOM Technical Report 91-C-038, 1992.

[3] A combined surface integral and finite element solution for a three-dimensional contact problem, S. Vijayakar, *International Journal for Numerical Methods in Engineering*, vol.31, pp. 525-545, 1991.

[4] *Nonlinear and dynamic programming*, G. Hadley, Addison Wesley Publishing company, 1964.

[5] *Linear programming*, George Hadley, Addison Wesley, 1962.

[6] *Linear and Combinatorial Programming*, Katta G. Murty, John Wiley, 1976 ISBN: 0-471-57370-1.

[7] Linearization of multibody frictional contact problems, S. Vijayakar, H. Busby and D. Houser, *Computers and Structures*, vol. 29, no. 4, pp. 569-576, 1987.

[8] *Natural Frequency Spectra and Vibration Modes of Planetary Gears*, Jian Lin and Robert Parker, 1998 ASME Design Engineering Technical Conference, September 1998, Atlanta Georgia.

[9] *Gear Dynamics Experiments, Part I: Characterization of Forced Response*, Blankenship and Kahraman, ASME 7th International Power Transmissions and Gearing Conference, San Diego, October 1996.

[10] *Gear Dynamics Experiments, Part II: Effect of Involute Contact Ratio*, Blankenship and Kahraman, ASME 7th International Power Transmissions and Gearing Conference, San Diego, October 1996.

[11] *Gear Dynamics Experiments, Part III: Effect of Involute Tip Relief*, Blankenship and Kahraman, ASME 7th International Power Transmissions and Gearing Conference, San Diego, October 1996.

[12] The use of boundary elements for the determination of the geometry factor, Vijayakar and Houser, 1986 *AGMA Fall Technical Meeting*, Paper no. 86-FTM-10.

[13] Finite element analysis of quasi-prismatic structures, S. Vijayakar, H. Busby and D. Houser, *International Journal for Numerical Methods in Engineering*, vol. 24, pp. 1461-1477, 1987.

[14] Edge effects in gear tooth contact, S. Vijayakar, *ASME 7th International Power Transmissions and Gearing Conference*, San Diego, October 1996.

[15] Vibration Measurements on Planetary Gears of Aircraft Turbine Engines, M. Botman, *AIAA Journal*, vol. 17, no. 5, 1980.

[16] Dynamic Tooth Loads in Epicyclic Gears, F. Cunliffe, J. D. Smith, and D.B. Welbourn, *J. Eng. Ind. Trans. ASME*, May 1974.

Chapter 4

Dynamic Analysis

4.0.1 Introduction

In this chapter, the results of dynamic analysis from Planetary2D are validated with results from analytical (lumped parameter) models, where available. The system considered is the last stage reduction unit of a helicopter transmission (this example is part of standard Planetary2D installation). In this configuration, the ring gear is fixed and the sun gear and the carrier are the input and output members respectively.

Two different models are considered for analysis. In the first model, the ring gear is press fitted to a rigid housing, while in the second model, the ring gear is attached to the housing through splines (lugs). The model with splines provides accurate contact boundary conditions, and the stress levels predicted by this model match with measured data as reported in an earlier chapter. Since analytical solutions do not exist for the second model, results from Planetary2D dynamic analysis are shown along with arguments justifying the observed results.

4.0.2 Free Vibration Modes

The free vibration modes of the planetary system are computed from an idealized lumped parameter model where in gears are rigid bodies interconnected by springs representing mesh stiffness and support bearings. The Matlab program `planet_modes.m` enables the user to compute the natural frequencies and modes. The GUI interface in Figure 4.1 allows for easy input of inertial properties, bearing/tooth stiffness and boundary conditions. To derive the equations of motion, it is necessary to transform the the body motions to a coordinate system with an axis along the line of contact to compute the spring deformation. The spring force along the line of action is then resolved back to the body coordinate system to yield the equations of motion. Mode shape animation helps with the visualization. The user is referred to [**?**] for details of the modeling and equations of motion. Here we briefly describe the important results.

The cyclic symmetry of planetary gears leads to repeated modes. There are at most *fifteen different natural frequencies* when the number of planets $N \geq 3$. Table 4.1 lists the natural frequencies and their multiplicity. Some interesting conclusions can be drawn from Table 4.1 and the associated mode shapes.

1. Six natural frequencies always have multiplicity $m = 1$ for any N. The vibration modes have *pure rotation* of sun, carrier and ring and are called *rotational modes*. *All planets have the same motion and move in phase*. In rotational modes, the tooth mesh forces are in phase. Due the symmetric geometry, the net force on sun, carrier and ring is zero, but the net moment is non-zero causing a rotational motion.

Table 4.1: Natural frequencies (Hz). $N = 4$ and free-free boundary conditions.

Multiplicity, m	Frequency, Hz
1	0
	1536
	1971
	2626
	7774
	13072
2	727
	1091
	1893
	2343
	7190
	10438
$N-3$	1808
	5964
	6982

2. Six natural frequencies always have multiplicity $m = 2$ for any N. These vibration modes have *pure translation* of sun, carrier and ring and are called *translational modes*. In translational modes, *opposite planets move out-of-phase* (for N even). Here, the net moment on the sun, carrier, and the ring is zero, but the total force is non-zero.

3. The remaining modes have multiplicity $N - 3$. The vibration modes are termed *planet modes* since the sun, carrier and ring are stationary. Only planet motion occurs in these modes. In this case,*adjacent planets move out-of-phase* (for N even). In these modes, both total force and moment on the sun, carrier and ring is zero.

These well defined eigensolution properties are useful for to explain selective participation of different classes of vibration modes in dynamic response [**?**, **?**].

4.0.3 Validation of Impulse Response Functions

Planetary2D directly yields the dynamic response. For the non-rotating system [ring fixed, input torque to the sun gear, output from carrier (carrier rotation fixed)], an impulse force/moment is applied to the sun bearing for a single time step. The time domain impulse response of carrier, ring and planets are computed using Planetary2D (use the session files `ImpulseResponseSunFx.ses` and `ImpulseResponseSunMz.ses` for these simulations). The time domain impulse response functions are converted into frequency domain transfer function via FFT techniques.

The natural frequencies of the participating modes are computed from the peaks in the transfer functions. Matlab program `fftresponse.m` can be used to plot the transfer functions and visualize the operating deflection shapes at any selected frequency. These natural frequency estimates are compared with the exact solutions from the lumped parameter model. In addition, Planetary2D transfer functions are compared with the responses from analytical modal superposition.

The driving point frequency responses due to force (x-direction) is shown in Figures 4.2. There is excellent agreement between the Planetary2D solution which computes the transient solution due to the impact excitation and the solution from the lumped parameter model, where the solution is computed in the frequency domain using modal superposition.

The natural frequency comparisons are shown in Table 4.2. In general, there is good agreement between Planetary2D and the analytical model. The natural frequency predictions of the lumped parameter model seem to be a bit on the higher side.

Table 4.2: Natural frequency comparison for the four planet gear system.

Natural Frequency, Hz	Planetary2D	Lumped Parameter Model	Difference (%)
Translation	803	825	-2.6
	1722	1833	-6.0
	2181	2325	-6.2
Rotation	1150	1243	-7.5
	1778	1903	-6.5

4.0.4 Dynamic Response Under Operating Conditions

To study the dynamic response of the planetary gear system under operating conditions, several dynamic analyses were conducted over a range of input speeds from 100-4200 RPM. In the configuration analyzed, a constant input torque of 16200 lbf-in is applied to the sun gear. Each analysis computes the response at a single speed, and is subdivided into several ranges to facilitate loading the system statically, a ramp up phase to bring the system to desired speed and a final range where the system is in steady state. The time series data in the steady state range is analyzed in the frequency domain. This analysis procedure is repeated for each speed.

The windows batch file `setup_runs.bat` automates setting up the directory structure for the speed sweep runs namely a unique folder for each speed and copies the input files that are required for the analysis. The windows batch file `start_batch_run.bat` performs the analysis at each speed.

Planetary2D outputs the body deflections and forces in text format in files `CARRIERBRGRES.DAT`, `CARRIERRES.DAT`, `HOUSINGRES.DAT`, `PINION1BRGRES.DAT`, `PINIONnRES.DAT`, `PINIONnBRGRES.DAT`, `RINGRES.DAT`, `SUNBRGRES.DAT`, `SUNRES.DAT`. This data was post-processed in Matlab to obtain the steady state frequency response amplitudes. Matlab M-files `post_process_calyx_data.m` and `process_order_plots.m` are developed for this purpose to view the spectrograms and the order maps from the speed sweep runs.

Planetary2D also also outputs the file `INPUTTHETA.DAT`, which contains the instantaneous input angle as a function of time. The utility program `generate_tacho.m` generates a specified number of pulses for one complete rotation of the input member, which can be used to perform adaptive resampling of the time domain data for order analysis.

In the model used for speed sweep runs (Model 2), the ring gear is connected to the housing by 50 splines or lugs. The natural frequencies of the system are changed due to the different boundary conditions, as clearly seen from the results of the numerical impact tests using Planetary2D. There is also some coupling between the translational modes and the rotational modes, in the sense that the motion of the sun, carrier and ring bodies in the translational mode will have a small amount of rotation as well. The natural frequency estimates are obtained from the peaks in the computed transfer functions, which can be plotted using the Matlab program `fftresponse`. The natural frequencies are shown in Table 4.3.

In a planetary system, tooth forces in all the meshes are periodic with the fundamental period T_{cycle}. However there is relative phase difference between the forces in different meshes. Since the excitation is periodic, the frequency content of the excitation is predominantly concentrated at the mesh frequency and its higher harmonics. The mesh frequency is proportional to the input speed. There is an amplification in response whenever a harmonic of the tooth mesh frequency

Table 4.3: Natural frequency comparison for the four planet gear system.

Natural Frequency, Hz	Splined Model	Fixed Ring Model
Translation	921	803
	1895	1722
	2227	2181
	2952	
	3532	
	4298	
Rotation	1143	1150
	2421	1778
	3121	

coincides with a system natural frequency. A splined model will have additional excitation at the spline passage frequency and its harmonics. In the current model, the ring gear (99 teeth) is connected to the housing through 50 splines. At a given speed, the fundamental spline pass frequency will be approximately one-half (50/99) of that of the tooth mesh frequency.

4.0.5 Results and Discussion

The spectrograms and the order colormaps for the translational and rotational deflections of the sun are shown in Figures 4.3 and 4.4. Several interesting physical phenomena can be observed from these figures.

From Figure 4.3, it is clear that only the odd harmonics of the mesh frequency are dominant in the sun translation response. At frequencies of 943 Hz and 2206 Hz corresponding to the first and third translational modes, there is an amplification if there is a coincidence with odd tooth mesh harmonic. These peaks in dynamic response correlate very well with the natural frequency prediction from the system impulse response shown in Table 4.3. The spline pass harmonics are (at roughly about half the tooth mesh frequency) evident in the response as well.

Similarly, in Figure 4.4 only the even harmonics of the tooth mesh frequency are dominant. Again, there is excellent correlation between the peaks in the dynamic response (at 1169 Hz and 2349 Hz, corresponding to the first and second rotational modes) and the natural frequencies predicted from numerical impact test. The spline pass harmonics are seen in the rotational response as well.

This peculiar behavior where particular modes are excited in some mesh harmonics but not others is consistent with analytical predictions and can be explained by a practice called *planet phasing*. A parameter k is defined as $k =$ mod (lZ_s/N), where l denotes the harmonic of the tooth mesh frequency, Z_s is the number of teeth on the sun gear and N denotes the number of planets. The planets in the four planet system are not equally spaced but lie along diameters. For even values of lZ_s translational modes are not excited and rotational modes are excited. For odd values of lZ_s, rotational modes are not excited, but translational modes are excited. Hence the results predicted by Planetary2D verify the theoretical predictions [**?**]. This knowledge is useful in the design stage to suppress either translational or rotational modes, by intentional phasing between the planets.

Figures 4.5 and 4.6 show the radial and rotational motions of one of the planets. All the tooth mesh harmonics and the spline passage harmonics participate in the planet motions, since for an individual planet participating in only two gear meshes the forces and moments do not cancel, unlike the sun gear.

The flexibility of the ring gear introduces additional dynamics at low frequencies. If the ring gear has uniform mass and stiffness, it can be shown that the exact shape of the mode

of vibration consists of a sinusoid along the ring circumference [**?**]. The exact formula for the natural frequencies is given as

$$\omega_n = \frac{n(n^2-1)}{\sqrt{n^2+1}}\sqrt{\frac{EI}{\mu_1 R^4}} \tag{4.1}$$

where $n > 1$ is the number of full waves, μ_1 is mass per unit length of the ring, EI is the bending stiffness and R is the ring radius. The mass per unit length of the ring gear is computed from Planetary2D by querying the total mass of the ring gear and dividing by its circumference. An effective cross-section moment of inertia is computed from the ring gear dimensions. The geometry parameters of the ring gear are shown in Table 4.4.

Table 4.4: Geometry parameters to compute ring gear natural frequencies.

Elastic Modulus, (N/m^2)	2.10E+11
Moment of Inertia of the Cross Section, (m^4)	1.21E-09
Mass Per Unit Length, (kg/m)	1.8926
Radius, (m)	0.17088

Table 4.5: Ring gear modes and natural frequencies.

Number of Full Waves n	Frequency, Hz
2	169.39
3	479.11
4	918.66
5	1485.68
6	2179.46
7	2999.75
8	3946.43
9	5019.45
10	6218.78

Figure 4.7 displays the ring gear translational response. It is seen that only the ring gear modes that have even number of full waves around the circumference are excited. More detailed study is required to explain the the physical reason behind phenomenon. One potential reason may be our system has even number of pinions (four). There is good correlation between the predicted and computed natural frequencies.

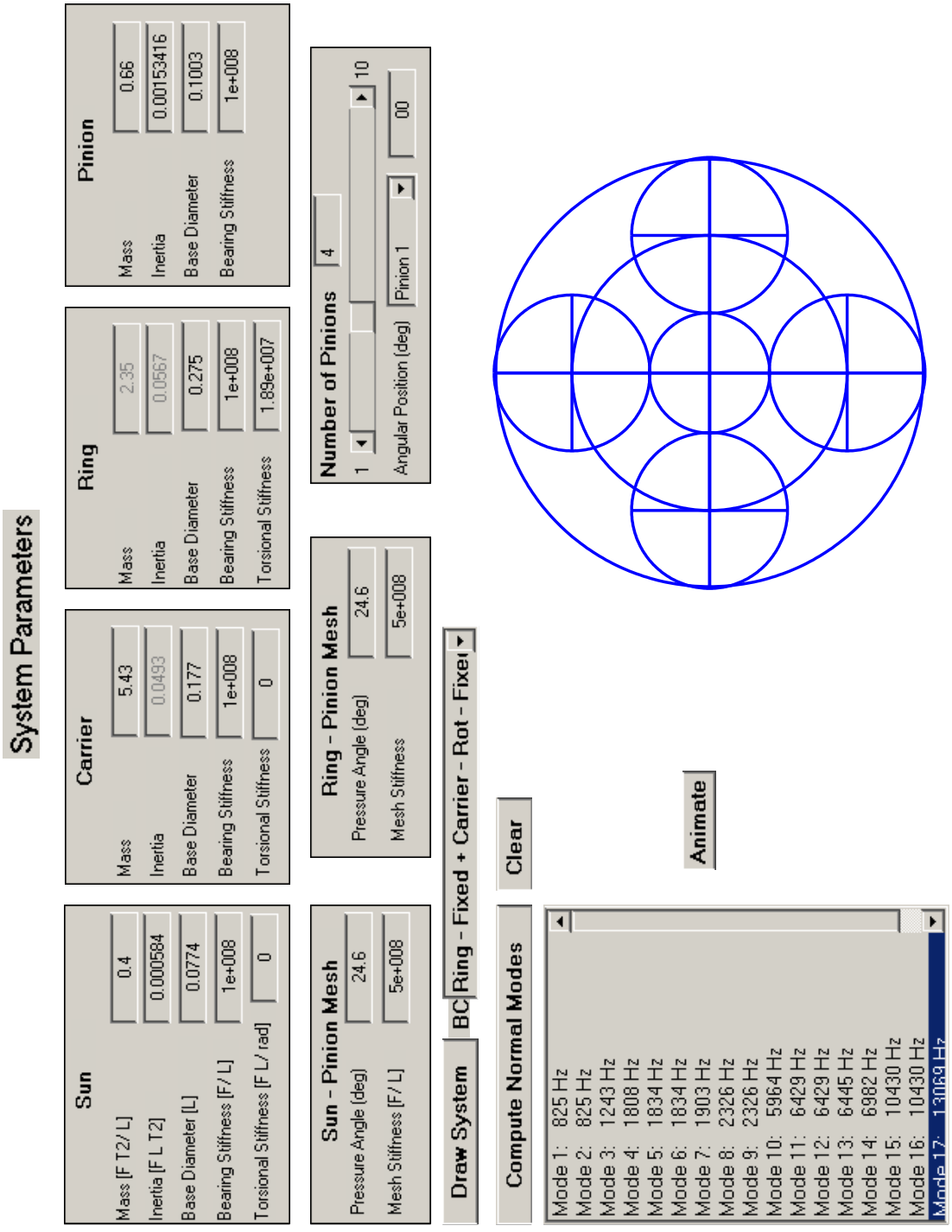

Figure 4.1: Matlab program for computing vibration modes of a planetary system.

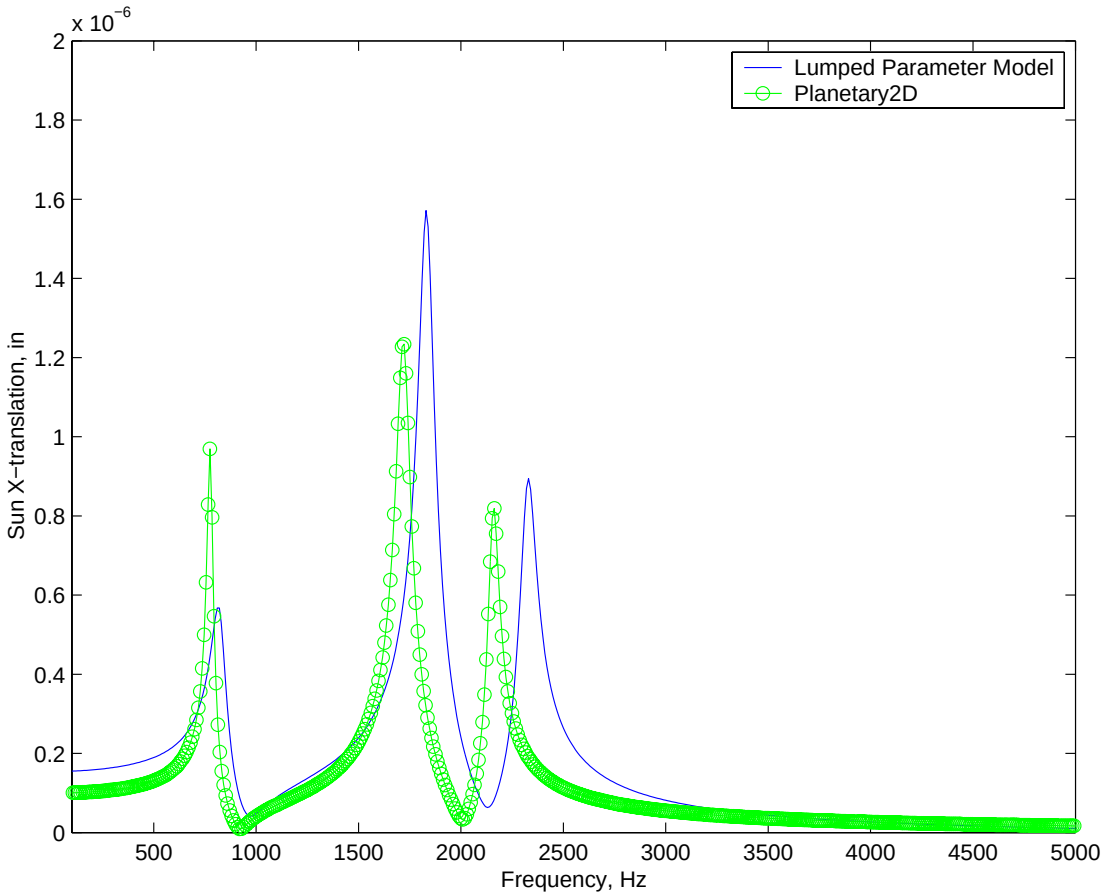

Figure 4.2: Driving point response – sun x-translation.

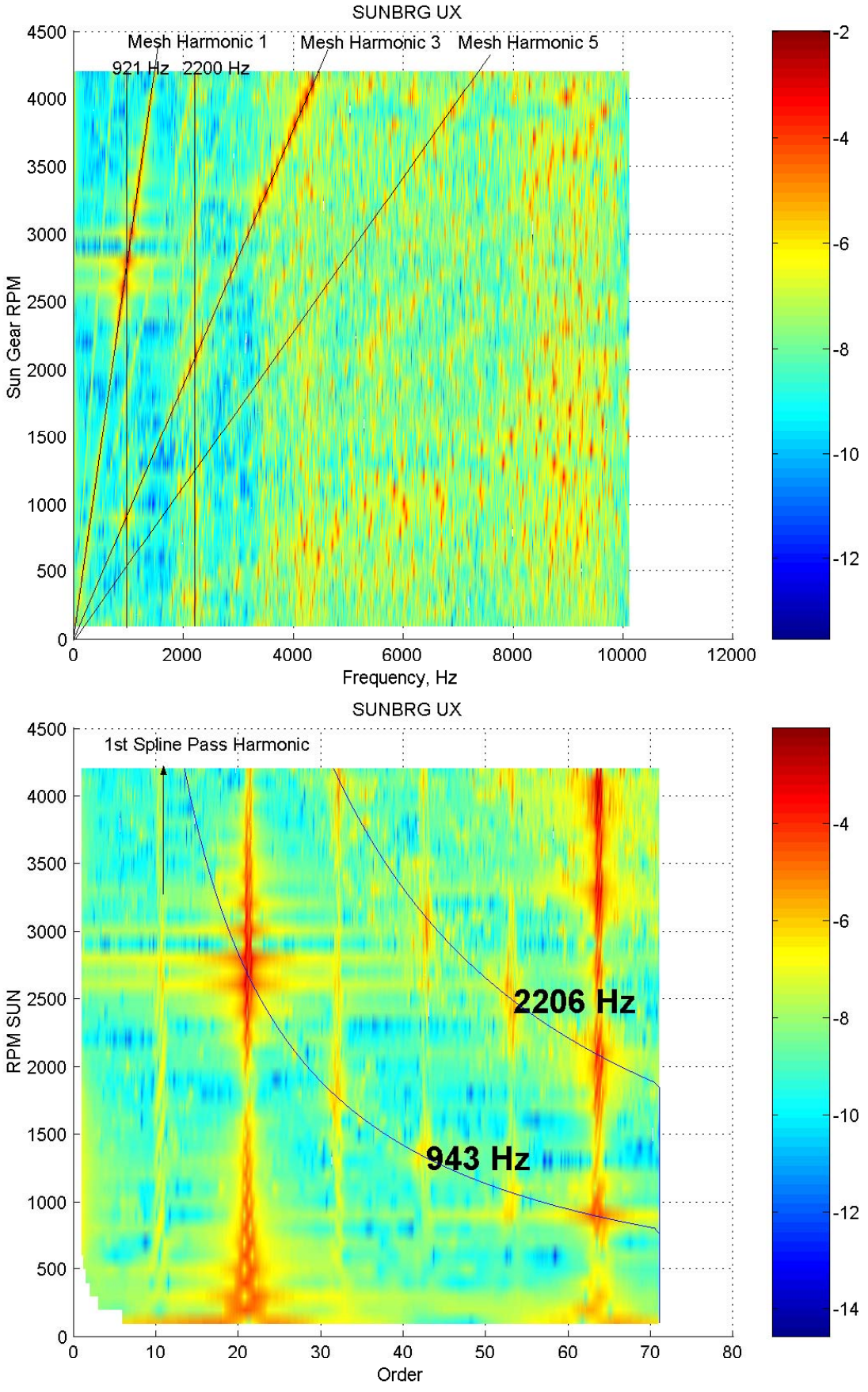

Figure 4.3: Frequency spectra of sun x-translation.

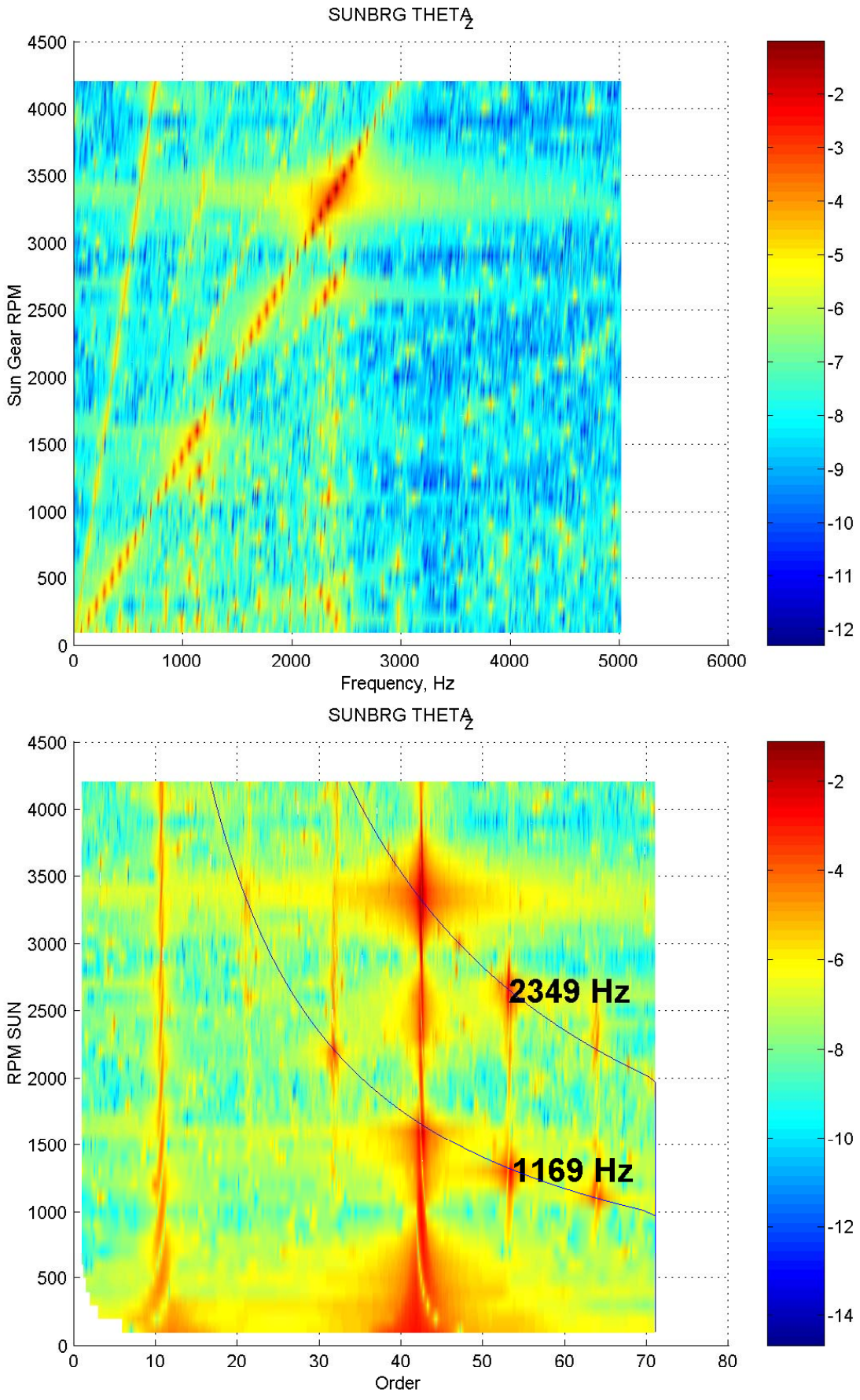

Figure 4.4: Frequency spectra of sun θ_z rotation.

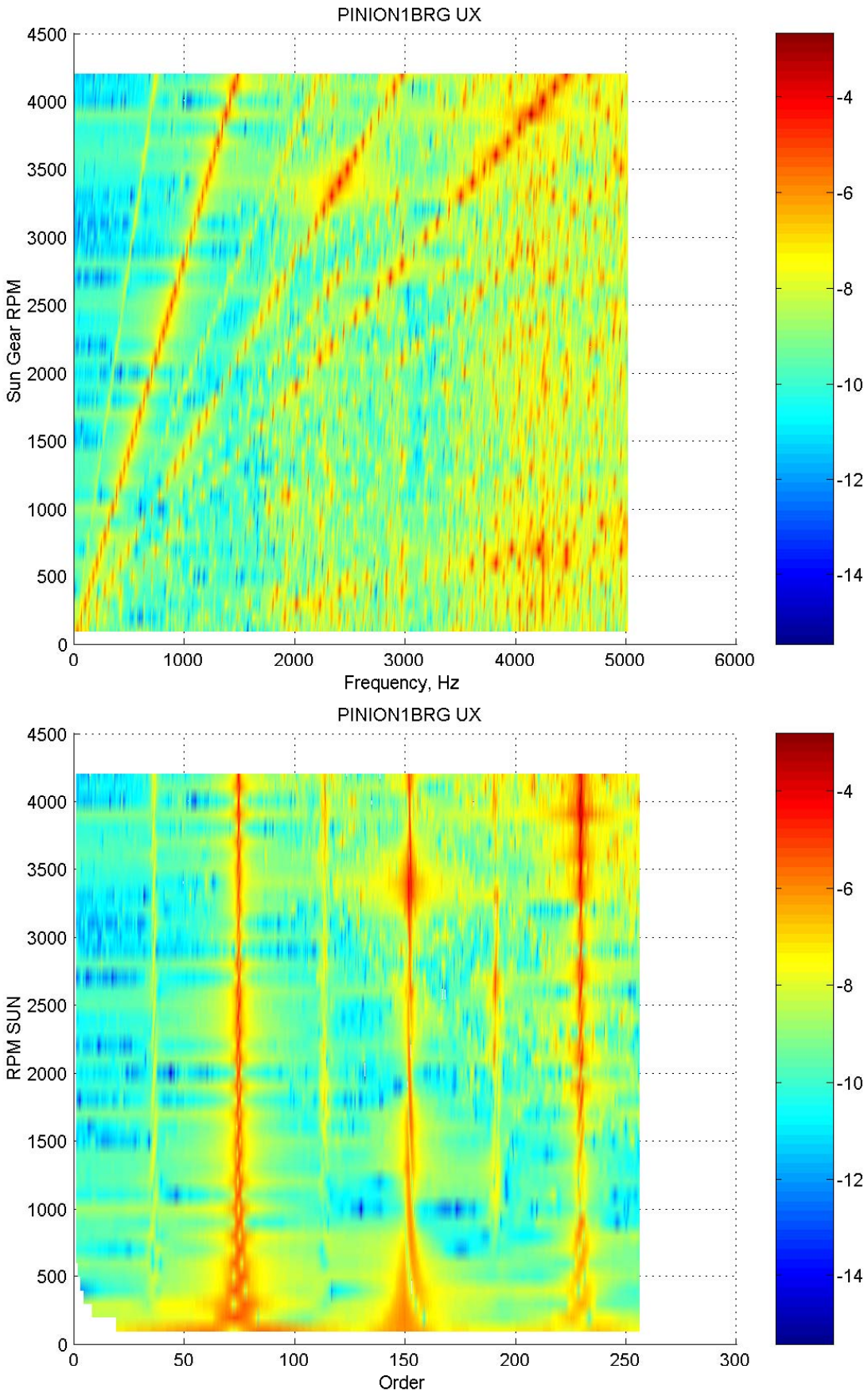

Figure 4.5: Frequency spectra of pinion radial translation.

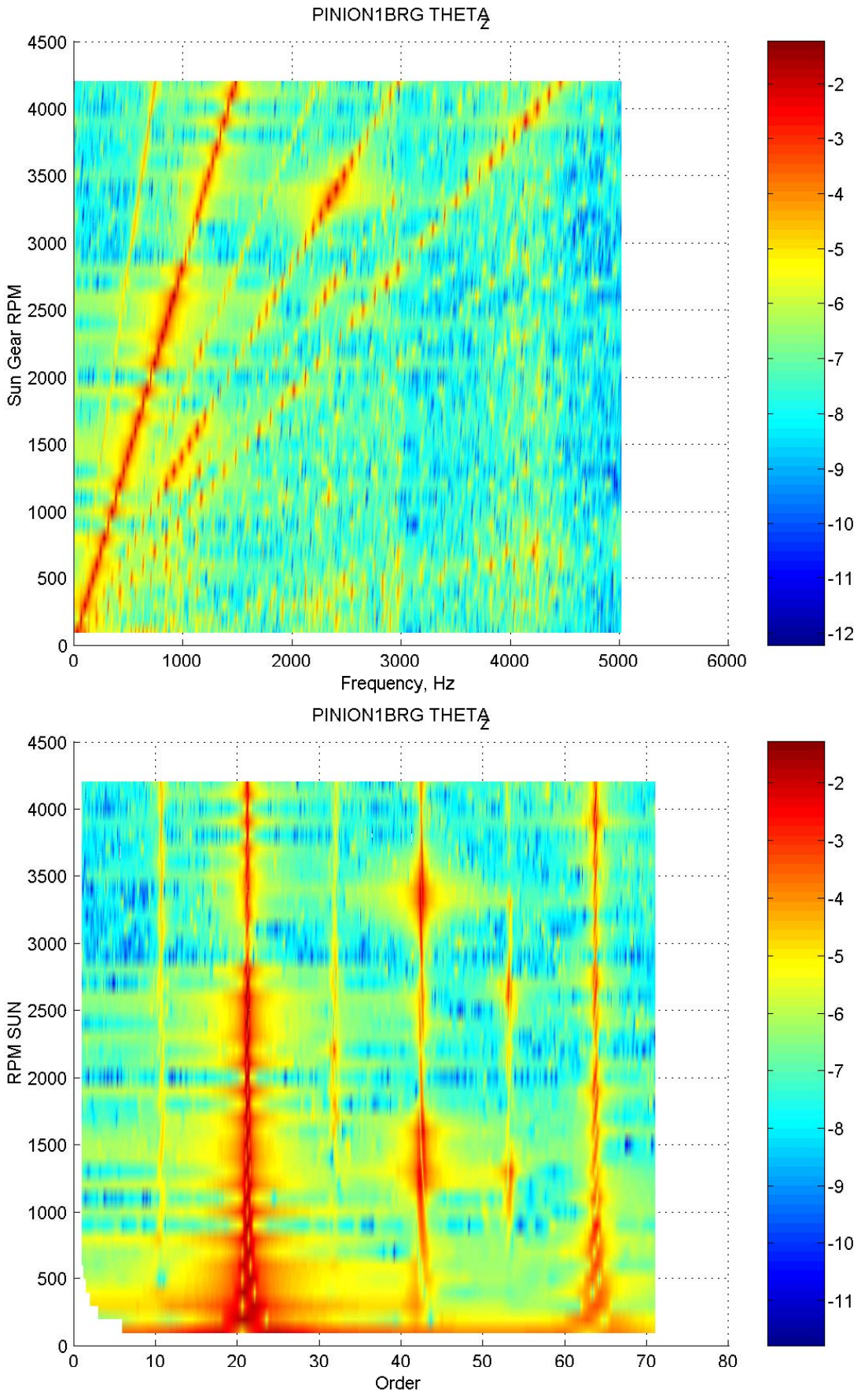

Figure 4.6: Frequency spectra of pinion rotation.

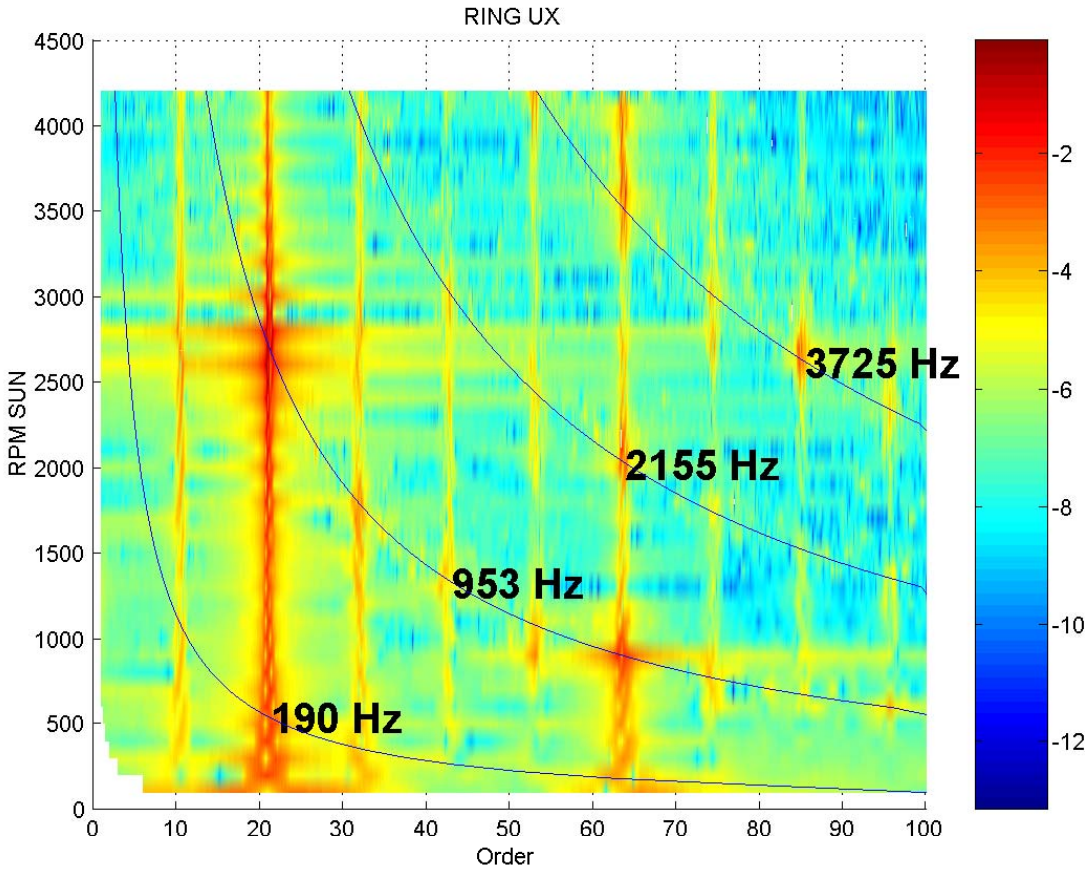

Figure 4.7: Frequency spectra of ring gear translation.

Chapter 5

Housing Vibration Spectra

5.1 Introduction

In most geared systems, the tooth meshing frequency and its harmonics dominate the vibration spectrum. In planetary systems the rotation of the carrier causes modulation sidebands at the carrier frequency (as measured by a transducer mounted on the stationary ring gear). In some cases the planetary gear vibration spectra exhibit considerable asymmetry of the modulation sidebands and even complete suppression of the tooth meshing harmonic. The theoretical explanation for this behavior is given by McFadden and Smith [**?**] and will be briefly summarized in Section 5.2. However, the main focus of this chapter is compare the results of a dynamic analysis performed using Planetary2D with theoretical predictions from [**?**].

The session file for the example used in this chapter is part of the Planetary2D installation. To run this example, load the session file `dynamicrun.ses` from the `housing_vibration_spectra` directory. The file `readme.txt` in the directory `housing_vibration_spectra` has additional information on setting up the ranges used in the dynamic analysis.

5.2 Theoretical Development

A epicyclic gearbox with a fixed ring gear is considered. The transducer is mounted on the stationary ring gear. N_r and N_s represent the numbers of teeth of the ring gear and the sun gear respectively. The speed ratio between the carrier and the sun is given by the formula

$$\frac{\omega_c}{\omega_s} = \frac{N_s}{N_s + N_r} \tag{5.1}$$

If the carrier speed ω_c is in rotations per minute (RPM), the carrier frequency f_c (in Hertz) is given as

$$f_c = \frac{\omega_c}{60} \tag{5.2}$$

The tooth meshing frequency f_x is related to the carrier frequency f_c and the ring frequency f_r through the number of ring gear teeth N_r.

$$f_x = N_r(f_c - f_r) \tag{5.3}$$

For a stationary ring gear $f_r = 0$, the above equation reduces to

$$f_x = N_r f_c \tag{5.4}$$

In the planetary gear system, the first planet can be located at any angular position (say at 0 degrees). After locating the first planet, the remaining planets locations are quantized. The

angular positions of the planets with respect to the first planet must be integer multiples of the least mesh angle δ.

$$\delta = \frac{2\pi}{N_s + N_r} = \frac{360}{N_s + N_r} \deg \tag{5.5}$$

The reasoning behind the computation of the least mesh angle δ is elegantly presented in the book by Muller [**?**]. The initial angular position of the nth pinion is given by ψ_n.

It is assumed that all meshes produce vibration of the same amplitude and phase, determined solely by the position of the teeth relative to the pitch point. The frequency of the nth sideband about the mth harmonic of the meshing frequency is given by

$$f_{mn} = mf_x + nf_c = (mN_r + n)f_c \tag{5.6}$$

Different planets in the same system have different phase angles relative to the first planet, and it is the relationship between the different phases produced by the planets that may cause the asymmetry in the observed spectrum. All the planets produce vibration of same magnitude, but a different phase. For a given mesh harmonic and sideband f_{mn}, the phase γ_i of the signal from a planet i (as measured by the transducer mounted on the stationary ring gear) is

$$\gamma_i = \frac{f_{mn}\psi_i}{f_c} = \psi_i(mN_r + n) \tag{5.7}$$

Therefore the frequency f_{mn} *will be present in the vibration spectrum only if* $\sum_{i=1}^{n} \exp(j\gamma_i)$ *is non-zero*. Among the frequency components that are present, this theory does not give any information of their relative magnitudes.

5.3 Validation

For the validation example, the US Army OH58 Kiowa Helicopter planetary is considered.

Table 5.1: Gear Parameters for example system

Sun Gear N_s	27			
Ring Gear N_r	99			
Pinion N_p	35			
Number of Planets n	4			
Angular Position of the Planets	0	$32\pi/63$	π	$95\pi/63$

In this example, all the planets are not equally spaced. However, opposite planets are 180 degrees apart.

A sun gear speed of $\omega_s = 1000\,\text{rpm}$ was used. This corresponds to a carrier frequency of $f_c = 3.571\,\text{Hz}$. The ring gear is constrained by fifty splines that are connected to the ground. The contact force on the spline is measured using a load sensor. The contact force time series data is converted into frequency domain to yield the vibration spectra.

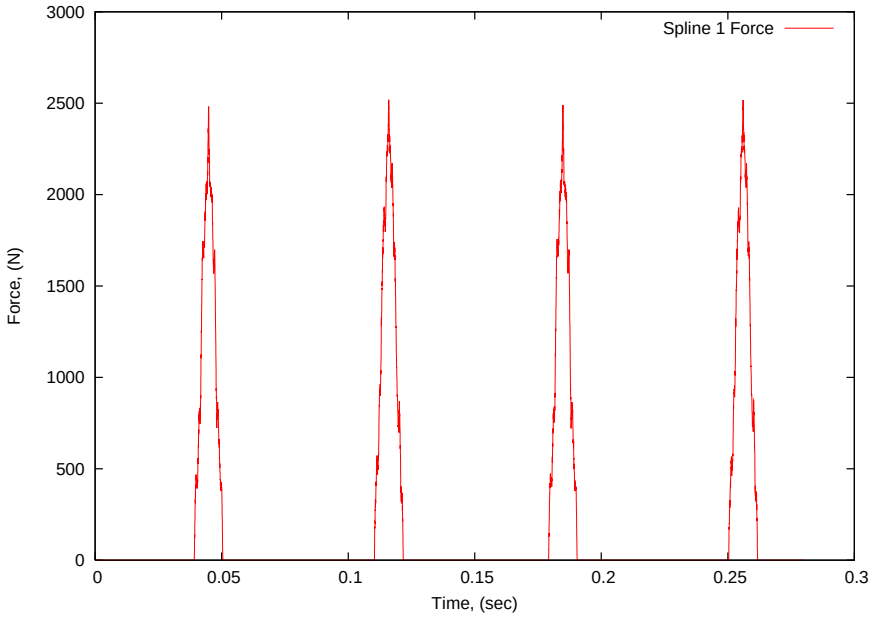

Figure 5.1: Force on Spline 1 over one complete rotation of the carrier

From Figure 5.1 it is seen that the as each pinion passes the spline, there is an spike in the load carried. In our numerical simulation, we used one hundred time steps within a tooth mesh cycle. Hence it is possible to capture the details of tooth mesh interactions adequately as shown in the following figure.

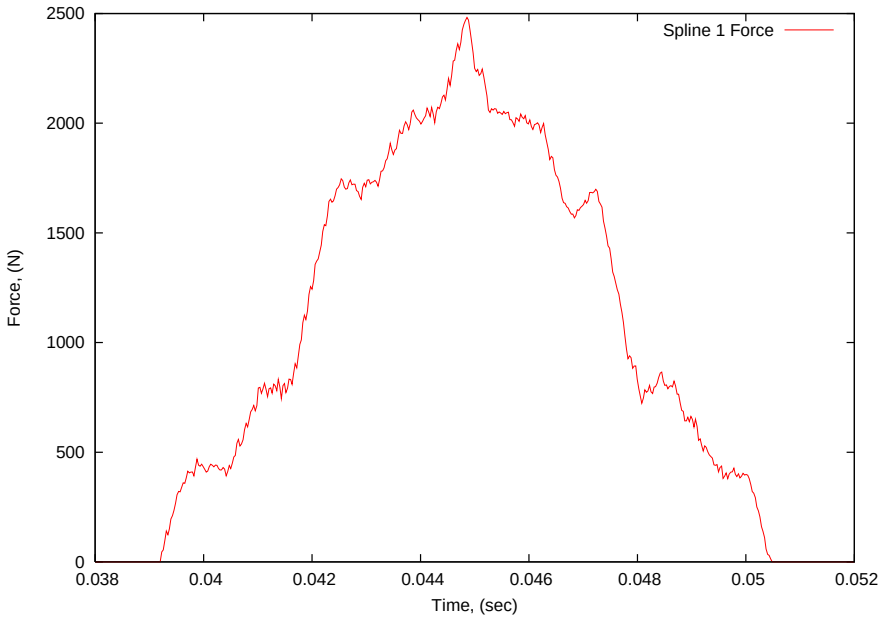

Figure 5.2: Force on Spline 1 as a planet passes the spline

The lug force spectrum in Figure 5.3 clearly shows the frequency components at mesh harmonics and their side bands. In Figure 5.3 the first two mesh harmonic frequencies are overlaid on the lug force spectra.

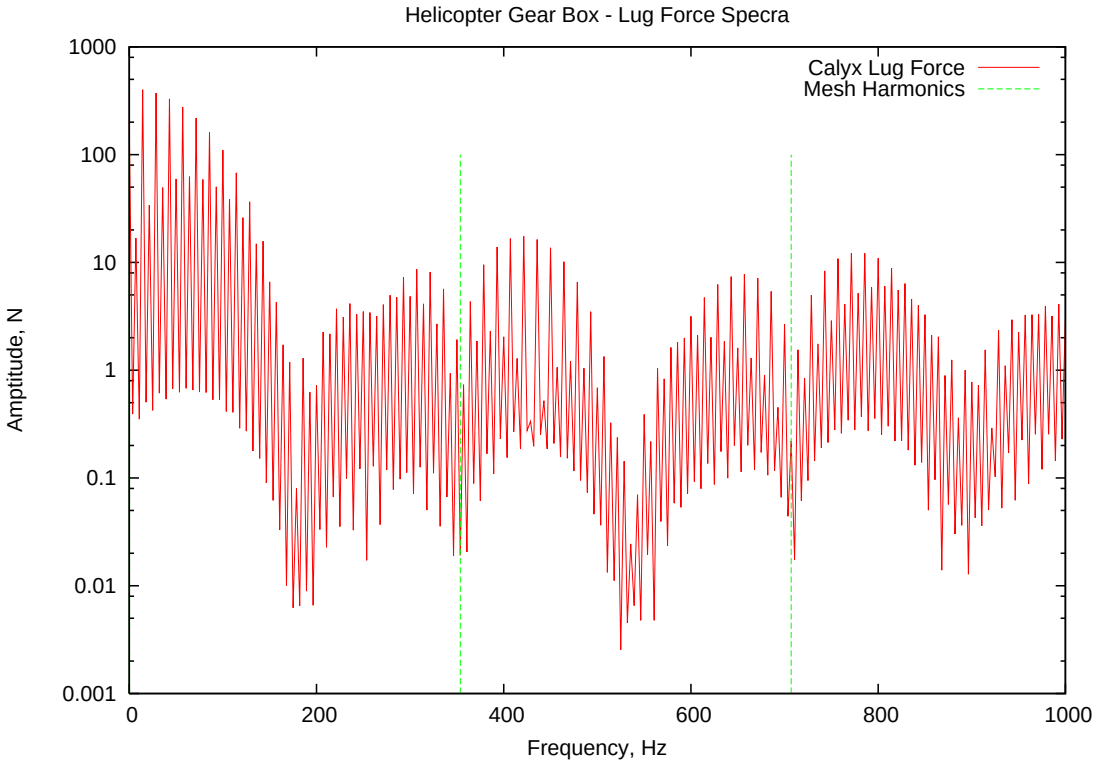

Figure 5.3: Force spectra on spline 1, 0-1000 Hz

We will examine the lug force spectra in detail, to validate if only the harmonics and side bands that are predicted by the theoretical model exist. Comparing Figure 5.4 and Table 5.2, it is evident that only the harmonics predicted by the theoretical model (even sidebands) are present in Planetary2D computed results.

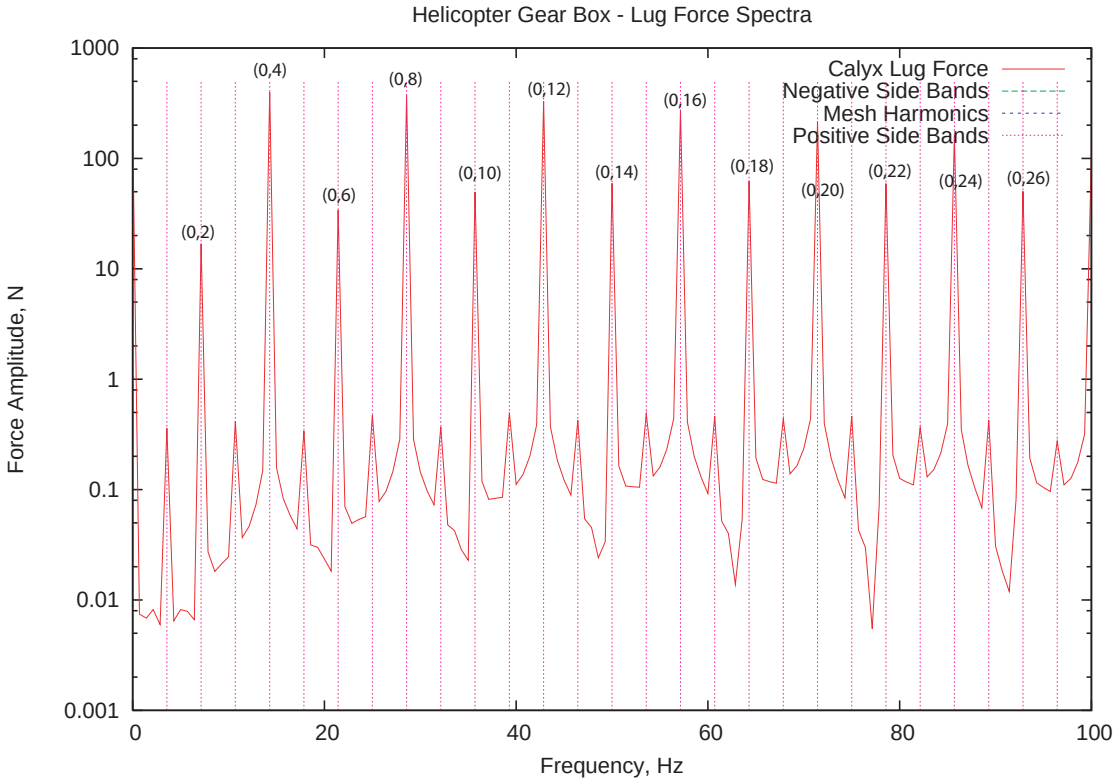

Figure 5.4: Force on Spline 1 around the zeroth mesh harmonic.

Table 5.2: Tooth harmonics and sidebands predicted by the theoretical model

Order	(0,0)	(0,1)	(0,2)	(0,3)	(0,4)	(0,5)	(0,6)	(0,7)	(0,8)	(0,9)	(0,10)
Frequency, Hz	0	3.57	7.14	10.71	14.29	17.86	21.43	25	28.57	32.14	35.71
Is Present	yes	no	yes	no	yes	no	yes	no	yes	no	yes
Order		(0,11)	(0,12)	(0,13)	(0,14)	(0,15)	(0,16)	(0,17)	(0,18)	(0,19)	(0,20)
Frequency, Hz		39.29	42.86	46.43	50	53.57	57.14	60.71	64.29	67.86	71.43
Is Present		no	yes	no	yes	no	yes	no	yes	no	yes
Order		(0,21)	(0,22)	(0,23)	(0,24)	(0,25)	(0,26)	(0,27)	(0,28)	(0,29)	(0,30)
Frequency, Hz		75	78.57	82.14	85.71	89.29	92.86	96.43	100	103.57	107.14
Is Present		no	yes	no	yes	no	yes	no	yes	no	yes
Order		(0,31)	(0,32)	(0,33)	(0,34)	(0,35)	(0,36)	(0,37)	(0,38)	(0,39)	(0,40)
Frequency, Hz		110.71	114.29	117.86	121.43	125	128.57	132.14	135.71	139.29	142.86
Is Present		no	yes	no	yes	no	yes	no	yes	no	yes

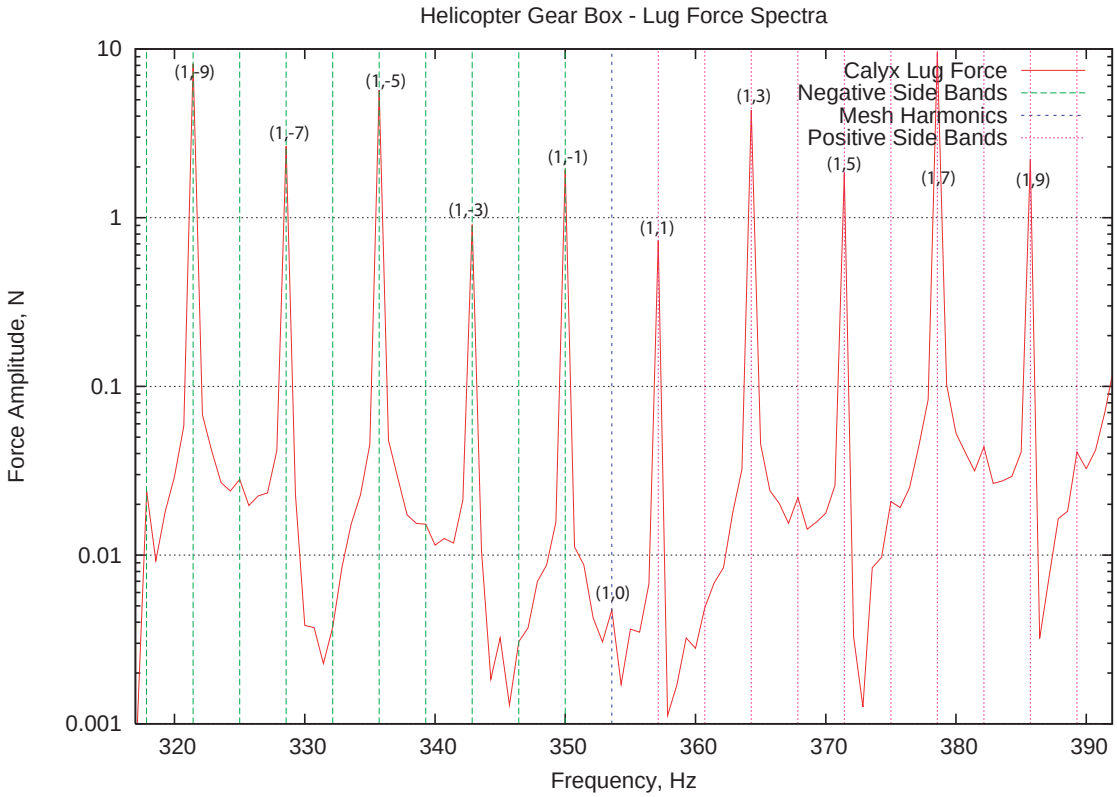

Figure 5.5: Force on Spline 1 around the first mesh harmonic.

Table 5.3: Tooth harmonics and sidebands predicted by the theoretical model

Order		(1,-1)	(1,-2)	(1,-3)	(1,-4)	(1,-5)	(1,-6)	(1,-7)	(1,-8)	(1,-9)	(1,-10)
Frequency, Hz		350.00	346.43	342.86	339.29	335.71	332.14	328.57	325.00	321.43	317.86
Is Present		yes	no	yes	no	yes	no	yes	no	yes	no
Order	(1,0)	(1,1)	(1,2)	(1,3)	(1,4)	(1,5)	(1,6)	(1,7)	(1,8)	(1,9)	(1,10)
Frequency, Hz	353.57	357.14	360.71	364.29	367.86	371.43	375.00	378.57	382.14	385.71	389.29
Is Present	no	yes	no	yes	no	yes	no	yes	no	yes	no

Comparing Figure 5.5 and Table 5.3, the first mesh harmonic is absent. Further only the odd sidebands around the first mesh harmonic are present in the lug force spectra.

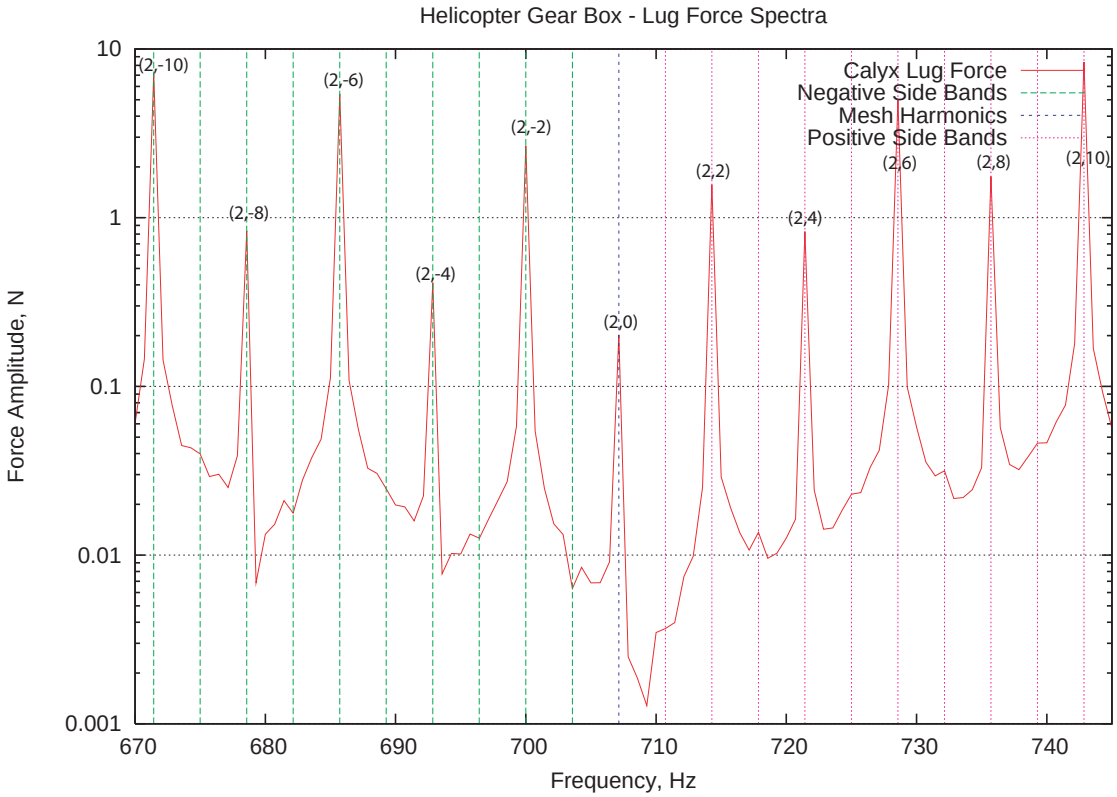

Figure 5.6: Force on Spline 1 around the second mesh harmonic.

Table 5.4: Tooth harmonics and sidebands predicted by the theoretical model

Order		(2,-1)	(2,-2)	(2,-3)	(2,-4)	(2,-5)	(2,-6)	(2,-7)	(2,-8)	(2,-9)	(2,-10)
Frequency, Hz		703.57	700.00	696.43	692.86	689.29	685.71	682.14	678.57	675.00	671.43
Is Present		no	yes	no	yes	no	yes	no	yes	no	yes
Order	(2,0)	(2,1)	(2,2)	(2,3)	(2,4)	(2,5)	(2,6)	(2,7)	(2,8)	(2,9)	(2,10)
Frequency, Hz	707.14	710.71	714.29	717.86	721.43	725.00	728.57	732.14	735.71	739.29	742.86
Is Present	yes	no	yes	no	yes	no	yes	no	yes	no	yes

Comparing Figure 5.6 and Table 5.4, only the second mesh harmonic and its even sidebands are present both in the theoretical prediction and the computed results.

5.4 Conclusion

A brief summary of the theoretical model for predicting the mesh harmonics and sideband orders in planetary gear vibration is presented. Using an example of a helicopter planetary gear box, we demonstrate that the computed spectra has the same mesh harmonics and sidebands as the theoretical model.

Chapter 6

Load Sharing Analysis

6.1 Introduction

This chapter describes the procedure used for computing the statistics of the load distribution among planets, given the various system errors and their statistics. The following system errors are considered - sun axis error (s_x, s_y), carrier axis error (c_x, c_y), ring axis error (r_x, r_y), and pin position error (p_r, p_t), thickness error (T), spacing error (Δ_s, Δ_r) and ring out of round errors (u_r) at each of the pinons. The input errors are considered to be independent random variables following a normal distribution.

Given the mean and standard deviation of the system errors, the Matlab program (based on a lumped parameter model) developed will allow us to compute the mean and standard deviation of the load carried by each pinion. The load sharing results from the lumped parameter model are compared with results from Planetary2D.

6.2 Modeling and Equations of Motion

In this section we derive the equations of motion for the planetary system consisting of spur gears, using a lumped parameter representation. The sun, carrier, ring, and all the planets are represented as rigid bodies. The central members may be connected to the ground via stiffness bearings. The pinions are connected to the carrier through stiffness bearings. Gear mesh forces are represented by linear springs along the line of action direction. Each of central members have two in-plane translations (x, y motions) and out-of-plane rotation θ_z. The planet deflections are described using radial and tangential cooridinates.

A schematic of the system is shown if Figure 6.1. In deriving the Equations of motion, we frequently encounter the following - To compute the spring (either mesh springs or bearing spring) forces, the motions of the two bodies connected by the spring must be resolved along the spring direction. Subsequently these forces must be resolved back along the body coordinate system directions for deriving the force balance equations. The transformation matrices that perform these are simple rotation matrices as shown in Figure 6.1.

The Equations of motion for the sun gear are as follows.

$$\begin{bmatrix} k_s & 0 & 0 \\ 0 & k_s & 0 \\ 0 & 0 & k_{s\theta} \end{bmatrix} \begin{Bmatrix} x_s \\ y_s \\ \theta_s \end{Bmatrix} + \sum_{i=1}^{N} k_{ms} \begin{bmatrix} \sin^2\psi_{sn} & -\sin\psi_{sn}\cos\psi_{sn} & -r_s\sin\psi_{sn} \\ -\sin\psi_{sn}\cos\psi_{sn} & \cos^2\psi_{sn} & r_s\cos\psi_{sn} \\ -r_s\sin\psi_{sn} & r_s\cos\psi_{sn} & r_s^2 \end{bmatrix} \begin{Bmatrix} x_s \\ y_s \\ \theta_s \end{Bmatrix} + \sum_{i=1}^{N} k_{ms} \begin{bmatrix} \sin\psi_{sn}\sin\alpha_s & \sin\psi_{sn}\cos\alpha_s & -r_1\sin\psi_{sn} \\ -\cos\psi_{sn}\sin\alpha_s & -\cos\psi_{sn}\cos\alpha_s & r_1\cos\psi_{sn} \\ -r_s\sin\alpha_s & -r_s\cos\alpha_s & r_1 r_s \end{bmatrix} \begin{Bmatrix} \xi_i \\ \eta_i \\ \theta_i \end{Bmatrix} = \begin{Bmatrix} F_{sx} \\ F_{sy} \\ T_{sz} \end{Bmatrix} \tag{6.1}$$

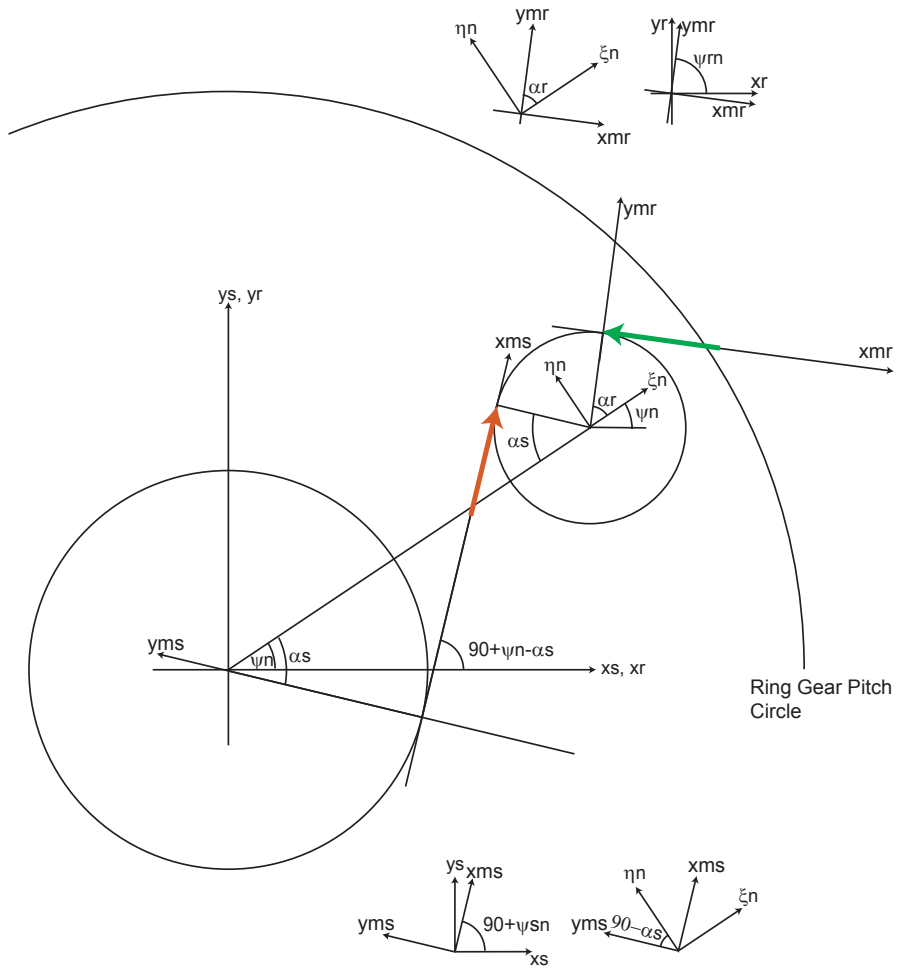

Figure 6.1: Lumped parameter model of the planetary gears and system coordinates.

Equations of motion for the ring gear are as follows.

$$\begin{bmatrix} k_r & 0 & 0 \\ 0 & k_r & 0 \\ 0 & 0 & k_{r\theta} \end{bmatrix} \begin{Bmatrix} x_r \\ y_r \\ \theta_r \end{Bmatrix} + \sum_{i=1}^{N} k_{mr} \begin{bmatrix} \sin^2\psi_{rn} & -\sin\psi_{rn}\cos\psi_{rn} & -r_r\sin\psi_{rn} \\ -\sin\psi_{rn}\cos\psi_{rn} & \cos^2\psi_{rn} & r_r\cos\psi_{rn} \\ -r_r\sin\psi_{rn} & r_r\cos\psi_{rn} & r_r^2 \end{bmatrix} \begin{Bmatrix} x_r \\ y_r \\ \theta_r \end{Bmatrix} + \sum_{i=1}^{N} k_{mr} \begin{bmatrix} -\sin\psi_{rn}\sin\alpha_r & \sin\psi_{rn}\cos\alpha_r & r_2\sin\psi_{rn} \\ \cos\psi_{rn}\sin\alpha_r & -\cos\psi_{rn}\cos\alpha_r & -r_2\cos\psi_{rn} \\ r_r\sin\alpha_r & -r_r\cos\alpha_r & -r_2 r_r \end{bmatrix} \begin{Bmatrix} \xi_i \\ \eta_i \\ \theta_i \end{Bmatrix} = \begin{Bmatrix} F_{rx} \\ F_{ry} \\ T_{rz} \end{Bmatrix} \tag{6.2}$$

The Equations of motion of the carrier are as follows.

$$\begin{bmatrix} k_c & 0 & 0 \\ 0 & k_c & 0 \\ 0 & 0 & k_{c\theta} \end{bmatrix} \begin{Bmatrix} x_c \\ y_c \\ \theta_c \end{Bmatrix} + \sum_{i=1}^{N} k_p \begin{bmatrix} 1 & 0 & -r_c\sin\psi_n \\ 0 & 1 & r_c\cos\psi_n \\ -r_c\sin\psi_n & r_c\cos\psi_n & r_c^2 \end{bmatrix} \begin{Bmatrix} x_c \\ y_c \\ \theta_c \end{Bmatrix} + \sum_{i=1}^{N} k_p \begin{bmatrix} -\cos\psi_n & \sin\psi_n & 0 \\ -\sin\psi_n & -\cos\psi_n & 0 \\ 0 & -r_c & 0 \end{bmatrix} \begin{Bmatrix} \xi_i \\ \eta_i \\ \theta_i \end{Bmatrix} = \begin{Bmatrix} F_{cx} \\ F_{cy} \\ T_{cz} \end{Bmatrix} \tag{6.3}$$

The Equations of motion of the pinion are as follows.

$$
\begin{aligned}
&\begin{bmatrix} k_p & 0 & 0 \\ 0 & k_p & 0 \\ 0 & 0 & 0 \end{bmatrix} \begin{Bmatrix} \xi_i \\ \eta_i \\ \theta_i \end{Bmatrix} + k_{ms} \begin{bmatrix} \sin^2\alpha_s & \sin\alpha_s\cos\alpha_s & -r_1\sin\alpha_s \\ \sin\alpha_s\cos\alpha_s & \cos^2\alpha_s & -r_1\cos\alpha_s \\ -r_1\sin\alpha_s & -r_1\cos\alpha_s & r_1^2 \end{bmatrix} \begin{Bmatrix} \xi_i \\ \eta_i \\ \theta_i \end{Bmatrix} + \\
&k_{mr} \begin{bmatrix} \sin^2\alpha_r & -\sin\alpha_r\cos\alpha_r & -r_2\sin\alpha_r \\ -\sin\alpha_r\cos\alpha_r & \cos^2\alpha_r & r_2\cos\alpha_r \\ -r_2\sin\alpha_r & r_2\cos\alpha_r & r_2^2 \end{bmatrix} \begin{Bmatrix} \xi_i \\ \eta_i \\ \theta_i \end{Bmatrix} + \\
&k_{ms} \begin{bmatrix} \sin\psi_{sn}\sin\alpha_s & -\cos\psi_{sn}\sin\alpha_s & -r_s\sin\alpha_s \\ \sin\psi_{sn}\cos\alpha_s & -\cos\psi_{sn}\cos\alpha_s & -r_s\cos\alpha_s \\ -r_1\sin\psi_{sn} & r_1\cos\psi_{sn} & r_1 r_s \end{bmatrix} \begin{Bmatrix} x_s \\ y_s \\ \theta_s \end{Bmatrix} + \\
&k_{mr} \begin{bmatrix} -\sin\psi_{rn}\sin\alpha_r & \cos\psi_{rn}\sin\alpha_r & r_r\sin\alpha_r \\ \sin\psi_{rn}\cos\alpha_r & -\cos\psi_{rn}\cos\alpha_r & -r_r\cos\alpha_r \\ r_2\sin\psi_{rn} & -r_2\cos\psi_{rn} & -r_2 r_r \end{bmatrix} \begin{Bmatrix} x_r \\ y_r \\ \theta_r \end{Bmatrix} + \\
&k_p \begin{bmatrix} -\cos\psi_n & -\sin\psi_n & 0 \\ \sin\psi_n & -\cos\psi_n & -r_c \\ 0 & 0 & 0 \end{bmatrix} \begin{Bmatrix} x_c \\ y_c \\ \theta_c \end{Bmatrix} = \begin{Bmatrix} F_{pr} \\ F_{pt} \\ T_{pz} \end{Bmatrix}
\end{aligned}
\tag{6.4}
$$

In the above equations, ψ_n is the angular position of the n-th pinion, $\psi_{sn} = \psi_n - \alpha_s$, $\psi_{rn} = \psi_n + \alpha_r$, r_s is the base radius of the sun gear, r_r is the base radius of the ring gear, r_c is the center distance. r_1 is the base radius of the pinion deck in mesh with the sun gear, r_2 is the base radius of the pinion deck in mesh with the ring gear. Equations of motion for all the bodies are assembled to form the global stiffness matrix $[K]$.

Let us define a parameter called **angular interference** for a pinion which is the interference caused by errors, referenced to an angular rotation of the pinion. This parameter is a function of the position errors for sun, ring, carrier, and pinion as well as tooth spacing errors, thickness errors and the ring out-of-round errors. Angular interference is a measure of angular deformation of the pinion, and is an indicator of the load carried by a given pinion - greater the angular interference greater the load carried by the pinion. It provides a common metric that facilitates comparison of the effect of various position errors. All combinations of spacing errors that yield the same angular interference at a pinion are equivalent. Angular interference at the n-th pinion is given as follows.

$$
\begin{aligned}
a(\psi_n) = \; & -\left[\frac{\sin\psi_{sn}}{r_1}\right] s_x + \left[\frac{\cos\psi_{sn}}{r_1}\right] s_y - \left[\frac{\sin\psi_{rn}}{r_2}\right] r_x + \left[\frac{\cos\psi_{rn}}{r_2}\right] r_y \\
& + \left[\frac{\sin\psi_{sn}}{r_1} + \frac{\sin\psi_{rn}}{r_2}\right] c_x - \left[\frac{\cos\psi_{sn}}{r_1} + \frac{\cos\psi_{rn}}{r_2}\right] c_y - \left[\frac{\sin\alpha_s}{r_1} - \frac{\sin\alpha_r}{r_2}\right] p_r \\
& - \left[\frac{\cos\alpha_s}{r_1} + \frac{\cos\alpha_r}{r_2}\right] p_t + \left[\frac{\cos\alpha_s}{r_1}\right] \Delta(n_1) - \left[\frac{\cos\alpha_r}{r_2}\right] \Delta(n_2) \\
& + \left[\frac{\cos\alpha_s}{r_1} + \frac{\cos\alpha_r}{r_2}\right] \frac{T}{2} - \left[\frac{\sin\alpha_r}{r_2}\right] u_r(\psi_n)
\end{aligned}
\tag{6.5}
$$

6.3 Load Sharing Calculation

A typical planetary system will have one output member (external torque is specified and the member is free to rotate), and two input members (rotation is fixed). The nominal deflections x_{nom} that result from the application of external torque is used to compute the forces in each of the sun planet meshes. The perturbations to this nominal load caused by various system errors are superposed to yield the actual load carried by the planet.

Suppose that the system errors cause an linear interference of ϵ units at the i-th pinion. The resulting excitation due to linear interference of the system is shown in Figure 6.2. The forces on the sun gear are given as

$$F_{\delta s} = \left\{ \begin{array}{c} k_{ms}\varepsilon \sin\psi_{sn} \\ -k_{ms}\varepsilon \cos\psi_{sn} \\ -k_{ms}\varepsilon r_s \end{array} \right\}$$

$$F_{\delta pn} = \left\{ \begin{array}{c} k_{ms}\varepsilon \sin\alpha_s \\ k_{ms}\varepsilon \cos\alpha_s \\ -k_{ms}\varepsilon r_1 \end{array} \right\}$$

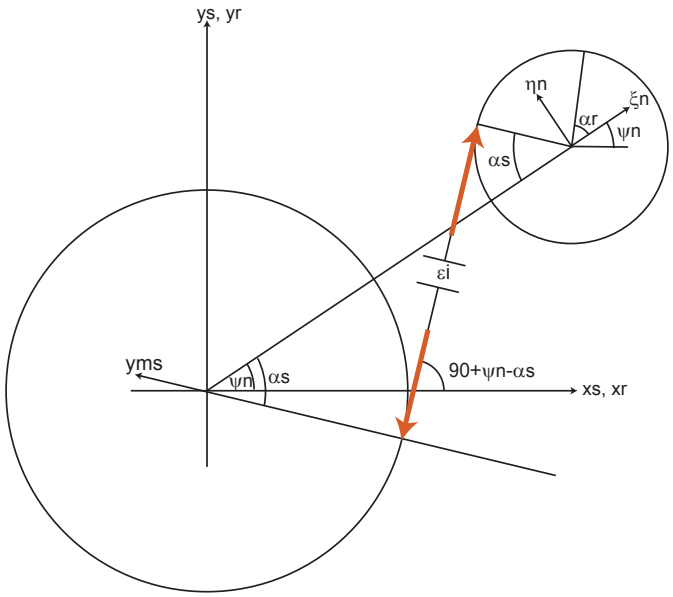

Figure 6.2: Excitation due to linear interference of ϵ at the planet i mesh

The perturbations to the motion $\{x_\delta\}$ is obtained by solving $[K]\{x_\delta\} = \{F_\delta\}$. Thus the forces in various sun planet meshes due to a linear interference of ϵ in mesh i is given by an equation of the form

$$\{F_m\} = \{F_{nom}\} + [A] \left\{ \begin{array}{c} 0 \\ 0 \\ \varepsilon_i \\ 0 \\ 0 \end{array} \right\} \tag{6.6}$$

In the above equation $[A]$ is related to the inverse of the system stiffness matrix $[K]$. The forces in various sun-planet meshes due to linear interferences in all the meshes is given as

$$\{F_m\} = \{F_{nom}\} + [A]\{\varepsilon\} \tag{6.7}$$

The linear interference in various sun-planet meshes due to the system errors is given by

means of Equation 6.5 as

$$\{\varepsilon\} = r_1 [B] \begin{Bmatrix} s_x \\ s_y \\ r_x \\ r_y \\ c_x \\ c_y \\ \overline{p}_r \\ \overline{p}_t \\ \overline{\Delta}(n_1) \\ \overline{\Delta}(n_2) \\ \overline{T} \\ \overline{u_r} \end{Bmatrix} = r_1 [B] \{\delta\} \tag{6.8}$$

Combining Equations 6.7 and 6.8 results in the expression that relates the load carried by each planet with the system errors.

$$\{F_m\} = \{F_{nom}\} + [A] \{\varepsilon\} = \{F_{nom}\} + [A] [B] \{\delta\} = \{F_{nom}\} + [C] \{\delta\} \tag{6.9}$$

6.3.1 Load Sharing Statistics

The mean value of load on each planet is given as

$$\{\langle F_m \rangle\} = \{F_{nom}\} + [C] \{\langle \delta \rangle\} \tag{6.10}$$

The standard deviation of load on each planet is given as

$$\{F_{m\sigma}\} = \sqrt{\left[C_{ij}^2\right] \{\delta_\sigma^2\}} \tag{6.11}$$

where δ_σ is the standard deviation of each error.

6.4 Implementation

A Matlab program that performs the load sharing analysis is developed. The GUI allows for easy input of the planetary system geometry, boundary conditions and various misalignments and errors. The ouput of the program is the load carried by each pinion.

To run the program, change the Matlab working directory to the folder containing the supplied files (`planet_load_sharing.m` and `planet_load_sharing.fig`) and type `planet_load_sharing` at the matlab prompt to bring up the program that performs the load sharing analysis.

6.5 Comparision with Lumped Parameter Model

The example case of US Army OH58 Kiowa Helicopter planetary is considered. The sun gear has an axis error of 0.005 in along the x-direction. The effect of the sun axis error on the planet load sharing is studies using Planetary2D and the lumped parameter model. The Planetary2D session file `load_sharing.ses` and the data for the matlab program `helicopter.mat` are in the folder `Load_Sharing_Model`. In Planetary2D the load carried by each pinion is computed from the bearing results files -`PINIONnBRGRES.DAT`, where n denotes the planet number. The following table compares the results of the two analyses.

From Table 6.5, it is clear that the load sharing trends compared to the nominal case for each of the planets are the same in both the models. For the position analyzed in Planetary2D,

Table 6.1: Planet load sharing in the Helicopter gearbox due to sun axis error

	Planetary2D	Lumped
Planet 1	28.83%	30.88%
Planet 2	16.92%	11.72%
Planet 3	21.97%	19.12%
Planet 4	32.27%	38.28%

the sun-planet1 and sun-planet2 mesh has one teeth in contact while the sun-planet3 and sun-planet4 meshes have two teeth in contact. Our lumped parameter model does not include the relative phasing in various sun-planet and ring-planet meshes and uses a constant mesh stiffness in all the sun-planet meshes, which accounts the difference in the load sharing percentage.

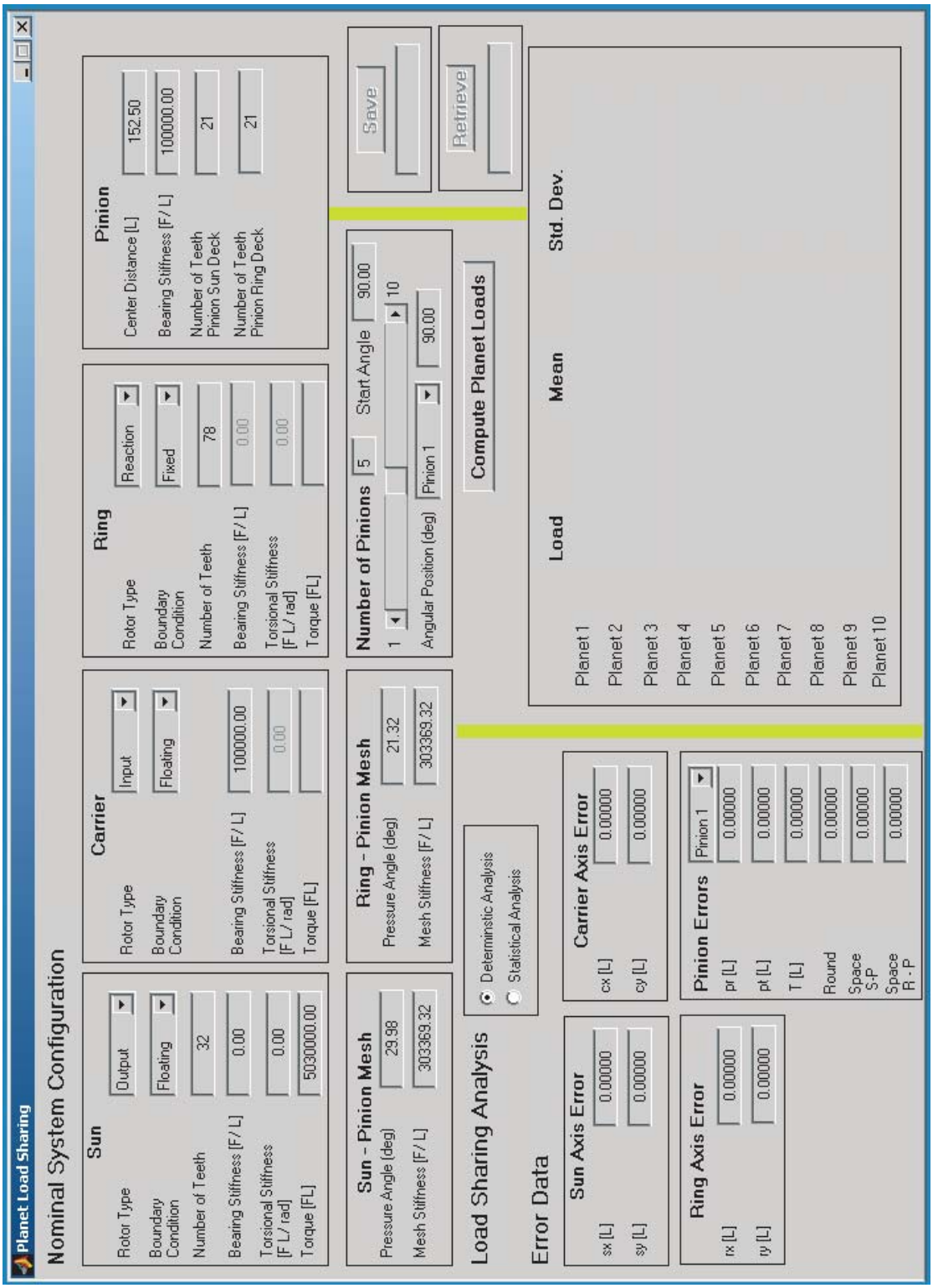

Figure 6.3: Software for load sharing analysis.